

## Article

# Research on Positioning and Simulation Method for Autonomous Mobile Construction Platform

Xinyu Shi <sup>1,2,\*</sup> , Chaoran Wang <sup>1</sup> , Tyson Keen Phillips <sup>3</sup> , Chengpeng Sun <sup>2</sup>, Haining Zhou <sup>2</sup> , Wenxuan Zhao <sup>1</sup>, Weijiu Cui <sup>1</sup> and Da Wan <sup>4,\*</sup> 

<sup>1</sup> iSMART, College of Architecture and Urban Planning, Qingdao University of Technology, Qingdao 266033, China

<sup>2</sup> Faculty of Environmental Engineering, The University of Kitakyushu, Fukuoka 808-0135, Japan

<sup>3</sup> Piaggio Fast Forward Co., Ltd., Boston, MA 02129, USA

<sup>4</sup> School of Architecture, Tianjin Chengjian University, Tianjin 300380, China

\* Correspondence: [sxy@qut.edu.cn](mailto:sxy@qut.edu.cn) (X.S.); [wanda@tcu.edu.cn](mailto:wanda@tcu.edu.cn) (D.W.); Tel.: +86-(0)532-8507-1127 (X.S.); +86-(0)22-2308-5067 (D.W.)

**Abstract:** In the architecture, engineering, and construction (AEC) industry, the positioning technology for a mobile construction platform (MCP) is critical to achieve on-site, continuous, large-scale construction. During construction, MCP movement and construction actions seldom occur simultaneously. Therefore, this paper categorizes the MCP into stationary and moving states for positioning studies, respectively. When the platform is stationary, it is positioned using an improved ultra-wideband (UWB) sensor. When the platform is in motion, a single UWB positioning technique cannot meet the required accuracy for positioning, and fusion positioning using both UWB and an inertial measurement unit (IMU) is considered. The experimental results show that compared with only UWB positioning, the improved UWB positioning algorithm improves the positioning accuracy by 53% in the stationary state, and the fused UWB/IMU positioning improves the positioning accuracy by 46% in the moving state. As a result, the positioning accuracy of the MCP is significantly improved regardless of whether it is in a stationary or moving state. Furthermore, this paper integrates the positioning technique with the robotic arm construction technique to successfully simulate an on-site continuous construction of a wooden cabin, which provides the potential for large-scale continuous construction in real-world scenarios in the future.

**Keywords:** mobile construction platform; UWB positioning; UWB/IMU fusion positioning; custom grasshopper plug-in; mobile construction simulation



**Citation:** Shi, X.; Wang, C.; Phillips, T.K.; Sun, C.; Zhou, H.; Zhao, W.; Cui, W.; Wan, D. Research on Positioning and Simulation Method for Autonomous Mobile Construction Platform. *Buildings* **2024**, *14*, 1196. <https://doi.org/10.3390/buildings14051196>

Academic Editor: Ahmed Senouci

Received: 15 March 2024

Revised: 15 April 2024

Accepted: 18 April 2024

Published: 23 April 2024



**Copyright:** © 2024 by the authors. Licensee MDPI, Basel, Switzerland. This article is an open access article distributed under the terms and conditions of the Creative Commons Attribution (CC BY) license (<https://creativecommons.org/licenses/by/4.0/>).

## 1. Introduction

Robotics is ushering in a golden age of rapid development, and mobile robotics in particular is receiving much attention from the industry. Currently, most robotic arms are fixed in a specific position to operate and their applications are limited to repetitive work in industrial production [1,2]. With the expansion of the robot application field, the environment faced by the robot is increasingly diversified, and the operation performed has a variety of uncertainties, which requires the robot to have the ability to move while also having specific operation abilities [3]. Therefore, the design of a mobile robotic arm can meet this demand. The so-called mobile robotic arm is installed on the intelligent mobile platform of the mobile robot, and the working space of the arm is expanded through the movement of the mobile platform. This structure enables the mobile robotic arm to have a larger operating room and a high degree of motion redundancy, combining the operability of the robotic arm and the mobility of the mobile platform, which is more adaptable to the changing environment and dramatically improves the robot's operable space, which makes it superior to the traditional robotic arm and has a broader application prospect [4].

In the applied research of mobile robotic arms, the robot's positioning technique is crucial to enable the robot to perform tasks accurately. In today's society, robots have become a valuable tool in many fields, including industrial production, healthcare, military applications, coordination, and service industries, and for robots to perform their tasks effectively, accurate positioning is crucial. Robots need to know exactly where they are and where they are headed in indoor or outdoor environments to navigate, avoid obstacles, perform tasks, and more. In outdoor environments, GPS can provide highly accurate navigation and positioning; however, in indoor environments, obstructions and reflections from buildings make positioning difficult. Many applications require reliable and precise positioning techniques in indoor environments, such as indoor pedestrian positioning and navigation, indoor UAV inspection, and indoor autonomous mobile robot positioning and navigation. Due to the complexity of indoor settings, indoor positioning systems need to overcome multipath and latency problems and cope with many non-line-of-sight and other wireless signal interference sources. Currently, the primary positioning techniques for mobile robots include GPS, Vision, LiDAR, UWB, and inertial navigation systems [5–7]. Among them, UWB technology has become the preferred method of positioning technology due to its advantages, such as its low cost, low power consumption, high transmission rate, robust security, and anti-interference. However, a single sensor is prone to excessive errors during mobile positioning, so multi-sensor fusion technology has become a new method to solve the unreliable positioning of a single sensor [8,9]. Therefore, the development and application of high-accuracy and reliable robot positioning technology is of great significance to promote the development of robot technology, improve work efficiency, reduce costs, and enhance safety and reliability.

In the AEC industry, many types of robotic automation construction are being used in an increasingly wide range of applications. Increasingly, mobile construction equipment is also being used to cope with the large-scale construction needs of buildings. In the mobile construction process, the positioning technology of an MCP has a significant impact on its construction effectiveness [10,11]. Most MCPs take construction actions when they are stationary, and they are rarely moving and under construction at the same time. Therefore, this paper analyzes the different states of the MCP and classifies them into stationary and mobile states for further research. In the stationary state, only UWB sensors are considered, and their positioning algorithms are improved to increase the positioning accuracy. In the mobile state, a single positioning technique cannot meet the demand of high accuracy positioning, so the multi-sensor fusion technique is used to improve the positioning accuracy [12]. In this paper, the raw UWB data are first preprocessed to suppress the effect of mutation values of UWB on fusion positioning, and the error-state Kalman filter (ESKF) algorithm fuses the positioning information of UWB and IMU in a tightly combined way, which takes advantage of the characteristics of no cumulative error of UWB and high short-term accuracy of IMU to provide more accurate positioning results when the UWB signals are weak or severely obscured, and suppresses the cumulative error of IMU and improves the positioning accuracy of UWB at the same time, therefore realizing the high-accuracy positioning of the MCP in the course of movement [13,14].

Based on this, this paper designs the positioning experiments of the MCP in stationary and moving states, which are carried out in 2D plane and 3D space, respectively. By comparing the positioning effects of various algorithms through multiple sets of positioning experiments, a reliable positioning algorithm applicable to both the stationary and moving states of the platform is obtained. The effectiveness of the proposed method is verified by transferring the above method to a KUKA-KR60 MCP equipped with a tracked chassis designated for the construction of wooden cabins. Considering that wood is the most common and renewable resource, this paper takes the construct of a wooden cabin as an example for the continuous construction simulation of MCP. The KUKA-KR60 used in this paper has an arm span of 210 cm, and the size of the wooden building is 330 cm × 400 cm × 420 cm. Therefore, it is necessary to combine the above positioning techniques with the specific task points of the MCP to realize the continuous construction of the MCP. This further

demonstrates that this study lays the foundation for realizing the continuous construction of large-scale models' on-site construction environments.

## 2. Literature Review

### 2.1. Mobile Intelligent Construction

As mobile robot technology continues to improve, increased researchers are working on developing mobile robots suitable for different tasks. For example, the Fraunhofer Institute developed a mobile robot [15], KUKA iisy, developed by KUKA, and the Spark robot, developed by NXROBO [16]. Robots suitable for the construction industry have not only demonstrated the potential to increase construction productivity but have also shown the ability to address issues such as labor shortages and safety risks in the construction sector [17,18]. Although robots have had enormous success in intelligent construction, this has only been for small scale components. When the goal of construction is large-scale components, robots can only build several small-sized components individually and then assemble them into large-scale components. Since the fabrication of large architectural structures exceeds the workspace of a stationary robot, this requires that the robot be mobile during the construction process and be able to orientate itself according to the workspace [19,20]. In order to solve this problem, professionals in the industry came up with the idea of combining a robotic arm with a mobile platform and started to investigate the coordination of the robotic arm and the mobile platform [21–24]. Yamamoto et al. [25] compensated for the dynamic interactions between the robotic arm and the mobile platform by using a nonlinear feedback control to give better co-ordination. The robot's positioning technique is particularly important in the mobile intelligent construction process. Therefore, more people have started to investigate different positioning methods. Norman et al. [26] used indoor GPS technology to achieve high-accuracy absolute positioning and motion of collaborative robots. Jiang et al. [27] developed a visual positioning system which consists of a camera and a video tracker. Susemihl et al. [28] proposed a new mobile robot system in order to process large aircraft parts. A laser tracker and a stereo camera are used for positioning, where the laser tracker is used to locate the position of the moving platform and the stereo camera system tracks the position of the robot end-effector.

In order to better apply mobile robotics to on-site construction, the ETH Zurich team has conducted a lot of attempts and experiments. Helm et al. [29] mounted an ABB IRB 4600 robot on a mobile platform to create a "dimRob" robot, which combines the constructability of the arm and the mobility of the mobile platform for 1:1 on-site manufacturing. Sandy et al. [10] proposed a repositioning system in order to address the limitations of robotics on construction sites, which uses only on-board sensors and allows the mobile robot to maintain a high degree of accuracy at multiple position in the construction task, demonstrating sub-centimeter repositioning accuracy by constructing vertical stacks of bricks in four different directions. Kathrin et al. [30] proposed the concept of an in situ fabricator (IF) based on the "dimRob" robot, where a 3D point cloud of the surrounding environment is constructed by mounting a laser range finder on the end-effector, which is accurately aligned with the initial point cloud to infer the relative position of the robot. A 6.5 m long and 2 m high double-leaf brick wall was constructed using the robot, and 14 repositionings were performed throughout the process. Due to the extreme flexibility of the camera, Lussi et al. [31] moved on to a vision-sensor-based solution, where the camera sensor was mounted on the robot's moving platform, scanning the AprilTag affixed to the floor for the robot's repositioning, and ultimately achieving millimeter-level positioning accuracy and replacing the laser scanner originally mounted on the end tooling with the camera to provide real-time feedback on the build tolerances, culminating in the fabrication of a lattice mold in the form of an S-shape that was 12 m in length. Gawel et al. [32] proposed a fully integrated sensor and control system for high-accuracy mobile robotic building construction, making it possible to enable robots to perform construction tasks with millimeter-level accuracy using LIDAR, IMUs, wheel encoders, and laser scanners. Hamner et al. [33] used a stereo camera as well as various

sensors to accomplish autonomous navigation and operation, enabling it to move and operate independently during assembly tasks. Chai et al. [34] used a depth camera to identify AprilTags, place sticks, and apply glue at specific positions to enable the operation of a mobile robot for on-site construction. If tags are used for positional recognition, it takes a long time to apply the tags and the camera is susceptible to the influence of the surrounding light environment, resulting in recognition errors. Wang et al. [35] verified the potential of integrating parametric design and robotic construction into wood building construction projects using the robotic construction of wood buildings as an orientation. In their study, a stationary robot was used to construct each unit horizontally on the ground, and then a crane was utilized to erect each unit and ultimately assemble them together for the construction of the entire building. However, this approach is limited by the working range of the robotic arm, as well as the inability to build directly on-site in the construction environment. Therefore, this paper is oriented towards large-scale constructions, using MCP to construct wooden cabins continuously in the vertical direction.

Dependable high-accuracy positioning is essential for mobile intelligent construction scenarios. Available positioning methods in intelligent construction, such as QR code-assisted positioning, are low-cost and easy to deploy. Still, the QR code on the ground is easy to wear out, requires regular maintenance, and has high requirements for ground flatness, so it is only suitable for use on factory floors. Laser scanning positioning technology involves much computing, and the surrounding environment must remain unchanged. Visual positioning uses a vision camera to capture images of the surrounding area, then calculates the position and direction of the surrounding environment, builds a map of the unknown territory, and then realizes the robot's positioning. Cameras are widely used because they are inexpensive and easy to operate. However, cameras are susceptible to light effects and produce erroneous images; for example, it takes work to identify the environment in dark environments. Therefore, to eliminate the above positioning limitations, this paper investigates various other positioning techniques for mobile robots to better apply them to mobile robot positioning.

## 2.2. Mobile Robot Positioning

Positioning techniques for mobile robots are crucial in performing tasks [36]. They ensure that the robot knows exactly where it is in the environment for task execution and navigation. Accurate positioning helps the robot to avoid obstacles, find the shortest path, and navigate in complex environments. In addition, positioning also motivates the robot to perceive objects and structures in the environment, identify and locate target objects, and interact with them. Overall, positioning technology for mobile robots is crucial for navigation, task execution, environment awareness, collaboration, and safety [37]. It improves the efficiency, reliability, and safety of robots, and enables them to better adapt to various environments. Therefore, more researchers are working on robot positioning techniques to improve positioning accuracy. On the one hand, the positioning accuracy of a single sensor is improved by improving the positioning algorithm to meet one's task requirements; on the other hand, the data from two or more sensors are fused to improve the robot's positioning accuracy.

Gentner et al. [38] used WIFI-round-trip-time for distance estimation of a target robot to achieve precise positioning. Xu et al. [39] achieved stable indoor positioning by extracting ceiling features with a camera mounted on an end tool. Jung et al. [40] proposed a SLAM approach where, by using a ceiling feature map, the A robot fitted with a monocular camera searches upwards for ceiling features and estimates the robot position using a Monte Carlo positioning method. Among the positioning techniques, UWB ranging systems stand out for their strong anti-jamming performance, high transmission rate, good multipath resistance, and high security [41], and they can achieve centimeter-level accuracy under line-of-sight conditions. Also, because UWB is deployed to achieve the positioning of the target node through the deployment of the base station, it is suitable for both indoor and outdoor applications, and thus has been favored by a large number of researchers. Richardson

et al. [42] analyzed the ranging accuracy of UWB and concluded that the ranging accuracy can reach up to 3 cm in the open outdoor environment. Li et al. [43] proposed a method to enhance UWB positioning using neural networks, and the experimental results show that neural networks can make UWB maintain stable positioning in both line-of-sight and non-line-of-sight scenarios. Takahara et al. [44] applied UWB positioning technology to the management of prison inmates, which can determine the position of the inmates in real time, and can improve the supervisory efficiency to a large extent. Ershadh et al. [45] proposed a design scheme to improve the antenna of UWB sensor, which enhances the comprehensive performance of UWB positioning under the unchanged spatial environment, but its high cost makes it unsuitable for large-scale popular application. Since single sensor positioning results may not be accurate enough in scenarios with extremely high accuracy requirements, increased research is focusing on multi-sensor fusion positioning techniques. Yang et al. [46] proposed a GA-BP neural network fusion UWB/IMU-based positioning method to address the problem of large error of a single positioning technique in complex indoor environments. The experimental results show that the GA-BP neural network fusion positioning method has a significant improvement in positioning accuracy over the single positioning method.

In multi-sensor fusion methods, Kalman filter (KF) is a commonly used tool for fusing data from different sensors. Since the KF algorithm was proposed in 1960 [47], researchers have proposed various improved algorithms based on KF [48], such as Extended KF (EKF) [49], Unscented KF (UKF) [50], Cubature KF (CKF) [51], etc. Woosik et al. [52] proposed a positioning method for data fusion of multiple low-cost GPS positioning systems using the EKF, thus improving the positioning accuracy of the system. Navarro et al. [53] used a tracking method based on EKF fusion of time-of-arrival and direction-of-arrival measurements of position. Liu et al. [54] proposed a method of fusion of UWB and IMU measurements using a CKF that corrects position, velocity, and orientation errors to improve orientation estimation and enhance the positioning accuracy of UWB. Agrawal et al. [55] proposed a low-cost positioning system consisting of stereo vision, IMU, and GPS, which achieved outdoor dm-level positioning accuracy by fusing information from these sensors through a KF. When the visual odometer fails, the IMU populates the motion estimation.

In summary, dependable high-accuracy positioning technology in mobile robotics is crucial for robot motion and navigation. When a single sensor cannot meet the requirements of a specific application scenario, multi-sensor data fusion positioning can be used to improve the robot's positioning accuracy. For different application scenarios, selecting appropriate sensors and positioning algorithms is crucial to ensure that the robot can achieve accurate positioning in various complex environments.

### 3. Methodology

#### 3.1. System Workflow of MCP

In order to achieve the subsequent continuous mobile construction, this paper combines a mobile platform positioning system with a robotic arm construction system, and the proposed mobile construction system design is shown in Figure 1. The host computer controls the control cabinet of the robotic arm online in real time through the mxAutomation plug-in to control the operation of the robotic arm, collects the raw data of positioning in the stationary and mobile states through the control of the mobile platform (which are then processed using the host computer to transmit the final positioning data to the mobile platform), and finally realizes the construction task of the MCP at a specific task point. In this case, the mxAutomation plug-in realizes the online control of the robotic arm by the host computer through UDP communication.

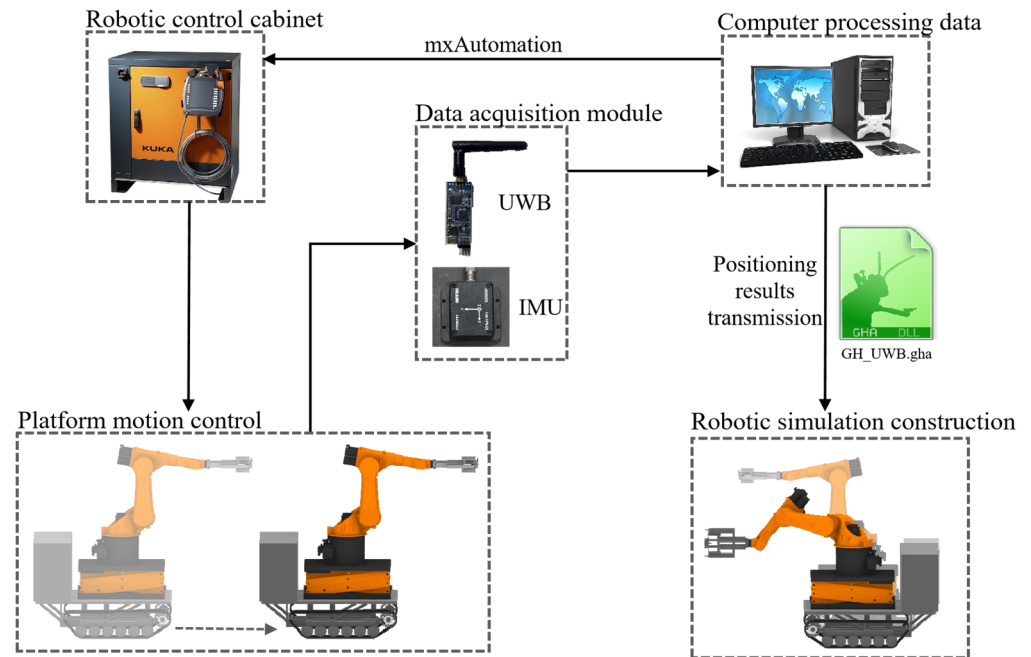


**Figure 1.** Mobile construction system.

The MCP is divided into two states, mobile and stationary, throughout the construction process. When the robotic arm reaches the initial task point, the robotic arm starts to carry out the construction operation. After completing the task at that task point, the arm starts moving to the next task point. Finally, the cycle repeats until the preset task is completed and the robotic arm stops working. Therefore, in this paper, it will be in accordance with the different states of the mobile platform in the construction process, with the robotic arm to build a large-scale model as an orientation and design the positioning experiments of the target nodes in the stationary and mobile states.

Wood, as a sustainable and renewable resource, is produced with low environmental impact and has excellent thermal insulation and humidity regulation properties to provide a comfortable environment for the occupants [56,57]. Research by Wang et al. [35] has successfully demonstrated the effectiveness of robots in erecting wood-frame constructions. Therefore, this paper has chosen to use the example of a wooden cabin to demonstrate the potential of MCPs in the continuous on-site construction of large-scale components. Figure 2 shows the specific dimensions of the large-scale target construction set in this paper. Based on this, the working range for positioning of MCP is set to be 400 cm × 600 cm.

Figure 3 shows the workflow diagram of the positioning system. Firstly, in the stationary state of the mobile platform, only UWB data are collected and pre-processed. The processed data are then fed into the positioning algorithm, and the positioning results are transferred in real time within Rhinoceros and transformed into a coordinate system via a customized Grasshopper (GH) plug-in, in order to obtain the positional information of the mobile platform in the world coordinate system. Secondly, during the travelling of the mobile platform to the next mission point, the UWB and IMU data are collected simultaneously, and data preprocessing is performed on them, respectively. Then, the processed data are transferred to the positioning algorithm to finally obtain the position information of the fused MCP. Finally, the positioning algorithm of the MCP in the stationary state is conjoined with the target building model to achieve continuous simulation of mobile construction.

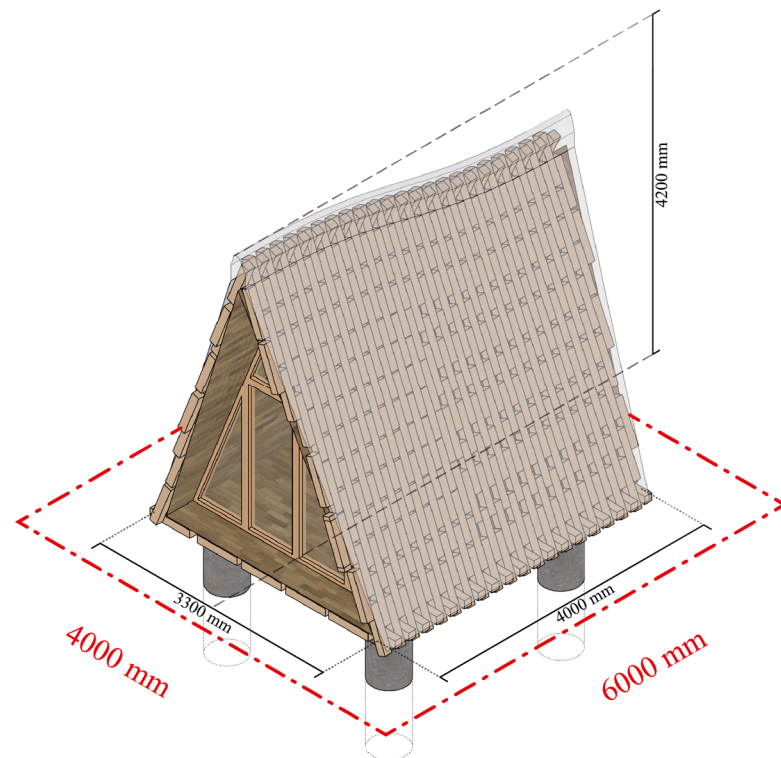


**Figure 2.** Schematic diagram of the full dimensions of the wood cabin.

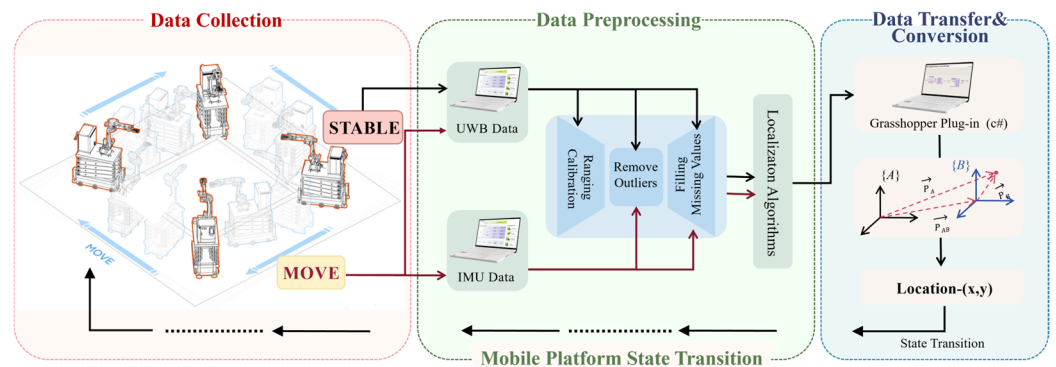


**Figure 3.** Diagram of positioning system workflow.

The results of the above positioning algorithm are based on the UWB coordinate system, while the robotic arm is based on the world coordinate system to build operations; however, when the robotic arm moves, it is not possible to accurately know the position of the robotic arm at this time under the world coordinate system, so it is necessary to convert the positioning results to coordinates. In this paper, the above improved UWB positioning results are written in C# language as a plug-in block recognizable by the KUKA robotic arm to obtain the position information of the robotic arm in the world coordinate system.

### 3.2. Positioning Coordinate Conversion

In the above description process, the position transformation technique is involved. Since the position description of any point in space is different in different coordinate systems, to convert the obtained positioning results to the position information of the robotic arm, it is necessary to transform the UWB coordinate system to the world coordinate system by the coordinate system. Through the translation and rotation of the coordinate axes, the position information about the robotic arm in the world coordinate system is finally obtained to correspond to the position information of the robotic arm in space and the actual position information. The detailed coordinate system transformation relationship is

shown in Figure 4, which contains three transformation relationships: translation, rotation, and translation and rotation.

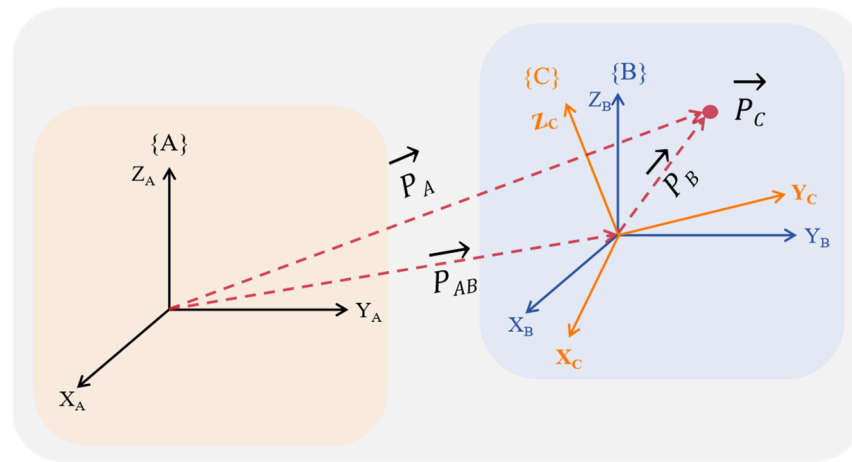


**Figure 4.** Coordinate system conversion diagram.

When the coordinate axes involve only translation transformations, such as the positional relationship between the coordinate system {A} and the coordinate system {B} in Figure 4, in order to transform the  $\vec{P}_B$  in the coordinate system {B} to the coordinate system {A}, that is, to describe this vector in the coordinate system {A}, the transformation relationship between the specific coordinate axes is Equation (1), where  $\vec{P}_B$  is the projection of this vector on each axis.

$$\vec{P}_A = \vec{P}_{AB} + \vec{P}_B \quad (1)$$

where the  $\vec{P}_B$  specific value is expressed as the projection  $\vec{P}_B = [p_{xb}, p_{yb}, p_{zb}]^T$  of this vector on each axis,  $\vec{P}_{AB}$  denotes the position vector of the origin of the coordinate system {B} in the coordinate system {A} and  $\vec{P}_A$  denotes the position vector of this point in the coordinate system {A}.

When the coordinate axes involve only rotational transformations, such as the positional relationship between the coordinate system {B} and the coordinate system {C} in Figure 4, in order to convert the  $\vec{P}_C$  in the coordinate system {C} to the vector  $\vec{P}_B$  in the coordinate system {B}, it is necessary to rotate the original coordinate axes, using the projection of each principal axis of this vector on each principal axis in the reference system {B} to represent it, and using the inner product of the  $s$  to find out the value of the projection of this vector in the coordinate system {B}.  ${}^B_C R$  denotes the rotational transformation from the coordinate system {C} to coordinate system {B}, and the detailed transformation relationship is shown in Equation (2).

$${}^B_C R = [{}^B X_C \quad {}^B Y_C \quad {}^B Z_C] = \begin{bmatrix} X_C \cdot X_B & Y_C \cdot X_B & Z_C \cdot X_B \\ X_C \cdot Y_B & Y_C \cdot Y_B & Z_C \cdot Y_B \\ X_C \cdot Z_B & Y_C \cdot Z_B & Z_C \cdot Z_B \end{bmatrix} \quad (2)$$

From this, it follows that

$$\vec{P}_B = {}^B_C R * \vec{P}_C \quad (3)$$

When the coordinate axes involve both translational and rotational transformations, such as the positional relationship between the coordinate system {C} and the coordinate system {A} in Figure 4, it is necessary to transform the coordinate system {C} to the transition

coordinate system {B} first, and then finally in the transformation to the coordinate system {A}, the transformation relationship between the coordinate systems is

$$\vec{P}_A = {}^B_C R * \vec{P}_C + \vec{P}_{AB} \quad (4)$$

### 3.3. MCP Positioning Data Collection and Processing

For the above-mentioned UWB and IMU positioning sensors, if the basic positioning algorithms are used, the positioning results are more dispersed and less accurate; therefore, this paper classifies the MCP into a stationary state and mobile state according to the state that exists during the construction process to be investigated separately.

#### 3.3.1. Data Preprocessing

In practice, the UWB sensor has a specific time error, and the electromagnetic wave will be affected by the surrounding environment in the transmission process, resulting in ranging errors. These ranging errors are the key reasons for the excessive positioning errors. Therefore, ranging calibration is needed before the experiment starts, to reduce the positioning error. The scenario is carried out under complete line-of-sight, where the UWB tags and the base station are placed at a fixed distance, as shown in Figure 5, and are divided into 20 groups based on 0~100 cm, moving the tags at 50 cm intervals, and 200 data are collected at each position. The average value is taken as the current measurement value. The specific distance measurement data of each class are shown in Figure 5. Linear fitting was performed on the above objective and measured distances, and the fitting results are shown in Figure 6.

As a result, a linear fitting relationship between the measured and actual values is obtained, and the ranging information of the UWB sensor is calibrated in conjunction with the  $x = (y - a)/b$  formula to obtain more accurate positioning information.

To ensure the stability of the positioning data, an additional 3–5 s of data are taken before and after the movement of the robotic arm, respectively. In the process of multi-sensor fusion, the processing of the time delay between data is essential. To make the state fusion of UWB and IMU sensor measurements more robust, the UWB and IMU data need to be time-aligned before fusion, i.e., the asynchronous measurement information of each sensor about the same target is synchronized to the exact moment. Since the sensors measure the target independently and often have different sampling periods, they often report to the data processing center at other moments. In addition, the time required to transfer information between the sensors and the fusion processing center varies due to further delays in the communication network. Since there may be a time difference in the sending time of the data on each sensor, the unsynchronized information needs to be aligned to the exact moment before the fusion processing to ensure that both UWB and IMU data are available at a particular moment. Too low a sampling frequency for the IMU leads to a side-long sampling period, which results in too large an error in the acceleration data through integration, so, in this paper, we set up the synchronization of data from both the UWB sensor and the IMU. The sampling frequency of the UWB sensor used in the experiment is 60 Hz, and the sampling frequency of the IMU sensor is 100 Hz. To synchronize the sampling frequency of the UWB sensor to that of the IMU, the first step is to process the ranging data of the UWB sensor, which includes setting a threshold value to exclude the abnormal data, arbitrarily selecting the data of 50 Hz from the original data, and equaling the data of the next moment to the data of the previous moment, to expand the data into 100 Hz data; the second step is to set up the data of the UWB and IMU sensors, which is the most suitable for the UWB 100 Hz data; secondly, the IMU acceleration and gyroscope data are processed, including rejecting abnormal data and filling in missing data.

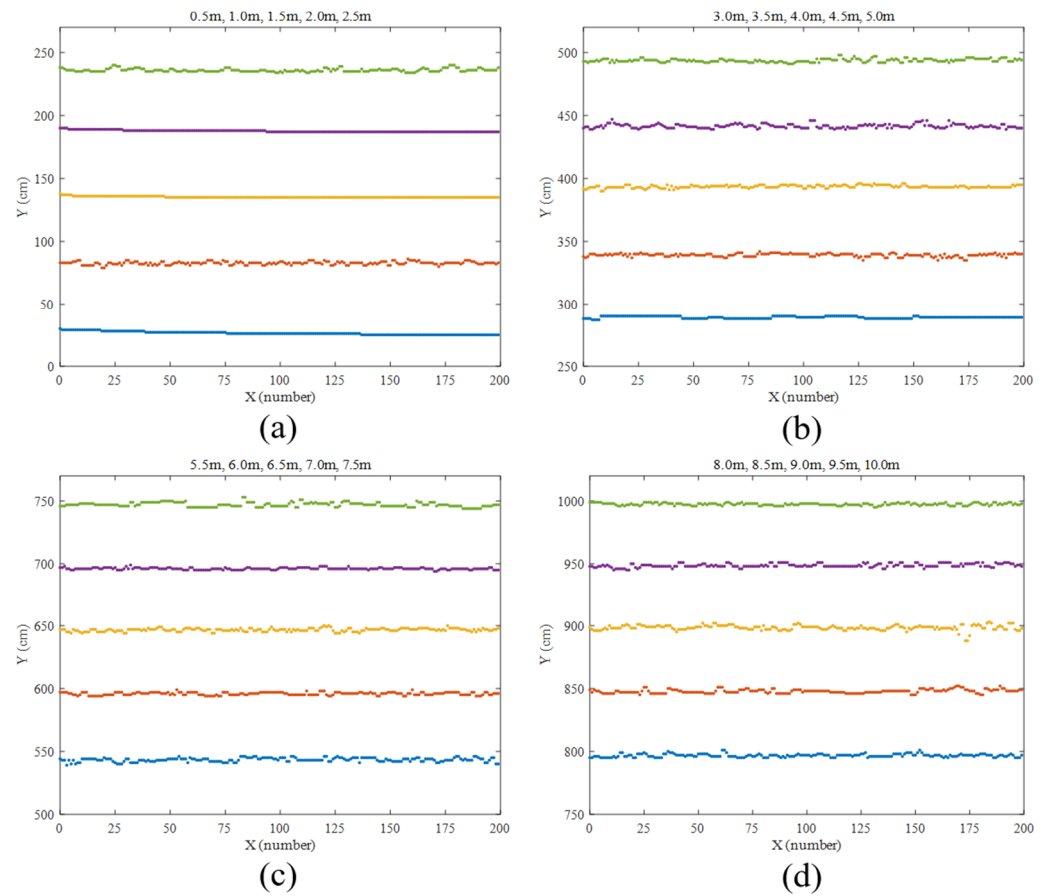


**Figure 5.** Distribution of base-A<sub>1</sub> to tag distance measurements. (a) Ranging results for 50 cm, 100 cm, 150 cm, 200 cm, 250 cm; (b) Ranging results for 300 cm, 350 cm, 400 cm, 450 cm, 500 cm; (c) Ranging results for 550 cm, 600 cm, 650 cm, 700 cm, 750 cm; (d) Ranging results for 800 cm, 850 cm, 900 cm, 950 cm, 1000 cm.

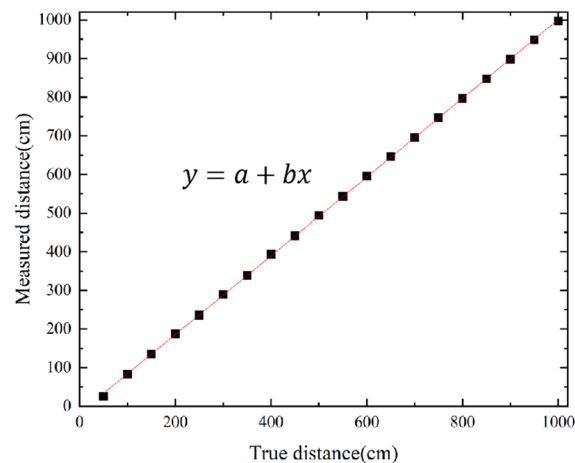


**Figure 6.** Results of linear fitting of true values to ranging values.

### 3.3.2. Improved LS Algorithm

In mobile intelligent construction scenarios, the robotic arm only starts the corresponding construction operation when the mobile robot is stationary. Hence, a stable positioning algorithm in the static state is fundamental. Since the positioning error of IMU grows infinitely with time, it is only suitable for fusing with other sensors for positioning within

a brief period or during motion. Therefore, in this paper, only UWB sensors are used for positioning when the mobile platform is stationary.

$$|d| = c * T_{\text{prop}}, c = 3 \times 10^8 \text{ m/s.} \quad (5)$$

UWB positioning usually calculates the distance based on the signal transmission time between the base station and the tag. Then, it uses the trilateral positioning algorithm to determine the target position. The traditional algorithms consist of the Chan algorithm based on TDOA, the least squares (LS) algorithm based on TOA, and the Taylor algorithm. The Chan algorithm has higher accuracy when the number of base stations is more significant, the least squares algorithm is simple in operation but has lower accuracy, and the Taylor algorithm has high accuracy, but its iteration time is longer and may not converge. Therefore, the least squares method is used in this paper for target position solving. In practical applications, due to the influence of the surrounding environment, relying on only three base stations for target positioning is likely to make the intersecting positioning area larger. Therefore, this paper uses four UWB base stations for the least squares positioning solution to reduce the positioning error. Figure 7 shows the schematic diagram of the multilateral positioning used in this paper.

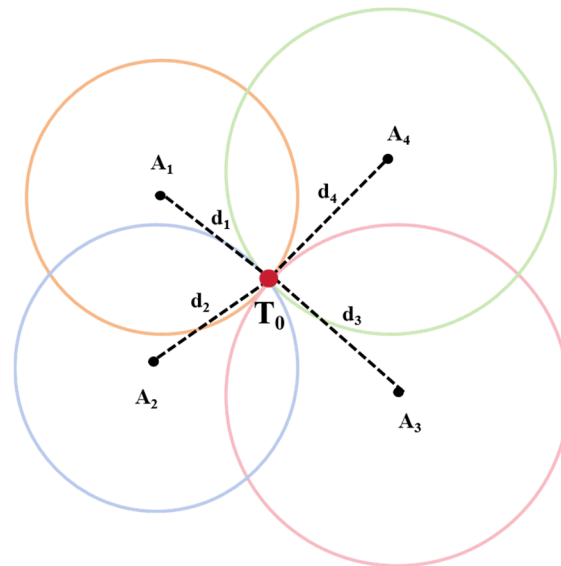


**Figure 7.** UWB multilateral positioning schematic.

UWB can obtain the distance from the tag to the fixed base station  $d_i$  ( $1 \leq i < 4$ ), where  $i$  is the serial number of the reference base station. The coordinates of the base station are  $(x_i, y_i)$ , and the coordinates of the target node are noted as  $T_0(x_0, y_0)$ . According to the distance calculation formula, a system of equations on the principle of ranging and positioning can be obtained as shown in Equation (6), and the position coordinates of the mobile tag can be obtained by solving this system of equations:

$$d_i^2 = (x_i - x_0)^2 + (y_i - y_0)^2, (i = 1, 2, 3, 4) \quad (6)$$

The solution is obtained from the following system of equations:

$$\begin{cases} d_2^2 - d_1^2 = x_2^2 - x_1^2 - 2(x_2 - x_1)x_0 + y_2^2 - y_1^2 - 2(y_2 - y_1)y_0 \\ d_3^2 - d_1^2 = x_3^2 - x_1^2 - 2(x_3 - x_1)x_0 + y_3^2 - y_1^2 - 2(y_3 - y_1)y_0 \\ d_4^2 - d_1^2 = x_4^2 - x_1^2 - 2(x_4 - x_1)x_0 + y_4^2 - y_1^2 - 2(y_4 - y_1)y_0 \end{cases} \quad (7)$$

Solve the above system of equations to solve for the position of the target node.

$$2 \begin{bmatrix} x_2 - x_1 & y_2 - y_1 \\ x_3 - x_1 & y_3 - y_1 \\ x_4 - x_1 & y_4 - y_1 \end{bmatrix} \begin{bmatrix} x_0 \\ y_0 \end{bmatrix} = \begin{bmatrix} (x_2^2 + y_2^2 - d_2^2) - (x_1^2 + y_1^2 - d_1^2) \\ (x_3^2 + y_3^2 - d_3^2) - (x_1^2 + y_1^2 - d_1^2) \\ (x_4^2 + y_4^2 - d_4^2) - (x_1^2 + y_1^2 - d_1^2) \end{bmatrix} \quad (8)$$

And convert to

$$AX = b \quad (9)$$

$$A = 2 \begin{bmatrix} x_2 - x_1 & y_2 - y_1 \\ x_3 - x_1 & y_3 - y_1 \\ x_4 - x_1 & y_4 - y_1 \end{bmatrix}, X = \begin{bmatrix} x_0 \\ y_0 \end{bmatrix}, b = \begin{bmatrix} (x_2^2 + y_2^2 - d_2^2) - (x_1^2 + y_1^2 - d_1^2) \\ (x_3^2 + y_3^2 - d_3^2) - (x_1^2 + y_1^2 - d_1^2) \\ (x_4^2 + y_4^2 - d_4^2) - (x_1^2 + y_1^2 - d_1^2) \end{bmatrix}.$$

Therefore, the solution results in

$$X = (A^T A)^{-1} A^T b \quad (10)$$

However, in the actual ranging process, the ranging error is unavoidable, and position solving only through the LS method is likely to lead to a positioning error that is too large for construction. The closer the distance to the tag after UWB ranging optimization, the smaller the error, and vice versa. Therefore, it is necessary to assign different weights to different base station tag distances. Based on this, this paper proposes to optimize the results solved by the original LS algorithm using the improved weighted LS (WLS) method.

A diagonal matrix  $W$  is added to the LS method, where the elements on the diagonal indicate different weight values assigned to each set of data.

$$W = \begin{bmatrix} w_{11} & 0 & 0 & 0 \\ 0 & w_{22} & 0 & 0 \\ 0 & 0 & w_{33} & 0 \\ 0 & 0 & 0 & w_{44} \end{bmatrix} \quad (11)$$

This results in a UWB solution of

$$X = (A^T W A)^{-1} A^T W b \quad (12)$$

In order to further improve the positioning accuracy, this paper adds the Taylor series expansion method on this basis to further reduce the positioning error. The Taylor series is a method based on the principle of Taylor expansion, which continuously corrects the initial position of the target node through recursion so as to gradually approximate the real position of the target node. Therefore, in this paper, under the stationary state of the mobile platform, a method of collaborative positioning using the WLS and the Taylor series (WLS-T) is proposed. In this method, the coordinates of the target node are calculated by the WLS method, then it is used as the initial value of the Taylor series algorithm, and finally, the coordinates of the target node are calculated again by the Taylor series algorithm, which gradually and iteratively converges to the real position coordinates.

Where the true position of the target node is  $(x, y)$ , the position coordinates calculated by the least squares method are used as the initial value  $\eta = (x_0, y_0)$ , and then

$$\begin{cases} x = x_0 + \Delta x \\ y = y_0 + \Delta y \end{cases} \quad (13)$$

In the case of 2D positioning, there are

$$d_i^2 = (x_i - x_0)^2 + (y_i - y_0)^2 = K_i + x_0^2 + y_0^2 - 2x_0x_i - 2y_0y_i \quad (14)$$

where  $\Delta x$  and  $\Delta y$  denotes the errors in the two directions, respectively. The Taylor series expansion of Equation (15) is conducted at  $(x_0, y_0)$  and the expansion terms of the second order and above are ignored, i.e.:

$$d_i = d_i|_{(x_0, y_0)} + \left. \frac{\partial d_i}{\partial x} \right|_{(x_0, y_0)} \Delta x + \left. \frac{\partial d_i}{\partial y} \right|_{(x_0, y_0)} \Delta y + \delta_i \quad (15)$$

where  $d_i|_{(x_0, y_0)} = \sqrt{(x_0 - x_i)^2 + (y_0 - y_i)^2}$ . In the iterative process,  $\Delta \eta = [\Delta x, \Delta y]^T$  the estimated value of the moving target is the iteration value. In the Taylor convergence process, make  $\eta = \eta + \Delta \eta$ . Continuously iterating to  $\sqrt{\Delta x^2 + \Delta y^2}$  until the accuracy requirements are met, an estimate of the final moving target  $\eta$  can be obtained.

### 3.3.3. Fusion Positioning Algorithm

Multi-sensor fusion can compensate for the shortcomings of a single positioning system, so multi-sensor fusion positioning is better than single sensor positioning in terms of positioning accuracy and stability. Because IMU is not affected by the external environment, it can achieve positioning only by itself, which can effectively overcome the random error in the process of UWB positioning, and the UWB positioning system can make up for the long-term drift error generated in the process of IMU positioning [58]. In the process of multi-sensor fusion positioning, KF, a specific implementation of Bayesian filtering, is widely used in the state estimation problem. However, KF can only be applied to linear systems, and most of the systems in the actual application scenarios are nonlinear, so the EKF was generated. When the EKF is in a particular state near the linearization of the system, the system is linearized. The direct method is used in EKF to linearize the system near a state, which can cause many problems. Therefore, based on the complementary characteristics of UWB and IMU positioning results in this paper, an ESKF [59] is proposed to fuse the positioning information from UWB and IMU sensors to improve the accuracy and stability of the positioning system.

The IMU is based on inertial sensor measurement and integration to achieve positioning. When the carrier is in motion, the accelerometer constantly outputs the acceleration of three axes, and the gyroscope constantly outputs the angular velocity of three axes. the angular velocity value is used to solve the direction angle of the accelerometer relative to the navigation coordinate system to obtain the rotation matrix, and then acquire the carrier's motion attitude and heading angle and other information. Then, the attitude matrix is used to convert the acceleration information to the navigation coordinate system and remove the gravitational acceleration. Finally, the primary integration is used to obtain the carrier's motion speed, and the secondary integration is used to contact the carrier's motion distance. In this paper, the Jetlink inertial navigation system is used. The gyroscope and accelerometer are solidly connected to the airline, and the principle of its navigation solution is shown in Figure 8.

In the process of coordinate transformation, the use of Euler angles is prone to the problem of gimbal deadlock, the use of rotation matrix needs to predefine the order of the rotation axis, and the use of quaternion only needs to calculate four elements, which is less computationally intensive and has less storage capacity, so, in this paper, we will use quaternion in the form of a quaternion to represent the transformation of the carrier coordinate system to the navigation coordinate system. Where the quaternion is defined as

$$q = q_0 + q_1i + q_2j + q_3k \quad (16)$$

where  $q_0, q_1, q_2$  and  $q_3$  are real numbers and  $i, j,$  and  $k$  are imaginary units and orthogonal to each other, it follows that the quaternion represents the rotation matrix from the carrier coordinate system, system  $b$ , to the navigation coordinate system, system  $n$ , as:

$$C_b^n = \begin{bmatrix} q_0^2 + q_1^2 - q_2^2 - q_3^2 & 2(q_1q_2 - q_0q_3) & 2(q_1q_3 + q_0q_2) \\ 2(q_1q_2 + q_0q_3) & q_0^2 - q_1^2 + q_2^2 - q_3^2 & 2(q_2q_3 - q_0q_1) \\ 2(q_1q_3 - q_0q_2) & 2(q_2q_3 + q_0q_1) & q_0^2 - q_1^2 - q_2^2 + q_3^2 \end{bmatrix} \quad (17)$$

Then, the gravitational acceleration is removed by rotational transformation, and the acceleration value is obtained in the navigation coordinate system.

$$a^n = \begin{bmatrix} a_x^n \\ a_y^n \\ a_z^n \end{bmatrix} - \begin{bmatrix} 0 \\ 0 \\ g \end{bmatrix} = C_b^n \begin{bmatrix} a_x^b \\ a_y^b \\ a_z^b \end{bmatrix} - \begin{bmatrix} 0 \\ 0 \\ g \end{bmatrix} \quad (18)$$

Finally, its primary integration yields the moving velocity of the platform, and its secondary integration delivers the displacement transformation, which is speculated to calculate the position coordinates at the next moment.

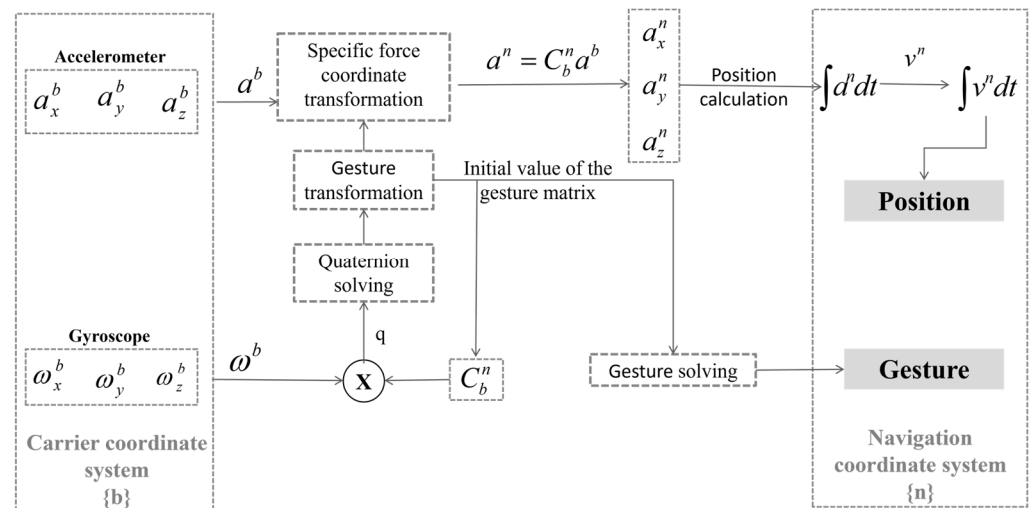


Figure 8. Block diagram of inertial navigation system.

When processing of UWB measurements is complete, the ESKF fusion process uses the IMU measurements as predictions for the filter and the UWB measurements as measurement updates for the filter. The algorithm integrates the IMU measurements when they arrive and puts them into the nominal state variable; at this time, the results do not consider various errors, so there is an error with the actual results. Thus, the error is estimated in real-time with the KF and put into the ESKF as an error variable. In this paper, UWB sensors are used for observation, and the error is calculated with the data from IMU. In the actual calculation process, the system state is divided into two parts, as shown in Equation (19):

$$X_t = X \oplus \delta X \quad (19)$$

where  $X_t$  is the system state truth value,  $X$  is Nominal state,  $\delta X$  is Error state. The first-order derivation of  $X_t$  is performed and the dynamics of  $X$  and  $\delta X$  are modelled separately as

$$\begin{cases} \dot{X} = f(X, u_m) \\ \dot{\delta X} = f_\delta(X, \delta X, u_m, i) \end{cases} \quad (20)$$

where  $u_m, i$  are the measured value of the IMU and the noise, respectively. Integrating the above equations and collapsing gives the error state and covariance matrix of the system as

$$\begin{cases} \delta X = F_\delta(X, u_m)\delta X \\ P = F_\delta P F_\delta^T + F_i Q_i F_i^T \end{cases} \quad (21)$$

When the IMU prediction is complete, the UWB data need to be fused at this point, setting the basic form of the UWB measurement equation as

$$y = h(X_t) + v, v \sim \mathcal{N}\{0, V\} \quad (22)$$

where  $y = [d1, d2, d3, d4]^T$  is the measured range between the four UWB base stations used in this paper and the target node.  $h(X_t)$  denotes the nonlinear functional relationship between the base stations and the target nodes, and  $v$  is the Gaussian white noise.

At this point, the KF is estimating the error state, and then the ESKF's measure update process is

$$\begin{cases} K = PH^T (HPH^T + V)^{-1} \\ \delta X = K(y - h(X_t)) \\ P = (I - KH)P \end{cases} \quad (23)$$

where the Jacobi matrix  $H$  is derived for the error state, i.e.:

$$H \triangleq \left. \frac{\partial h}{\partial \delta X} \right|_X = \left. \frac{\partial h}{\partial X_t} \right|_X \left. \frac{\partial X_t}{\partial \delta X} \right|_X = H_X X_{\delta X} \quad (24)$$

When the update of the error state is completed, the coordinates of the real position can be obtained, i.e., the values of the nominal state and the error state are merged.

$$X \leftarrow X \oplus \delta X \quad (25)$$

This results in a final ESKF calculated position and velocity of

$$\begin{cases} p \leftarrow p + \delta p \\ v \leftarrow v + \delta v \end{cases} \quad (26)$$

Finally, the error state is reset, and the covariance matrix  $P$  is updated, completing the cycle until the end.

$$\delta X \leftarrow 0 \quad (27)$$

$$P \leftarrow GPG^T \quad (28)$$

where  $G$  is the Jacobi matrix,  $G = I$ .

#### 4. Positioning Experiment and Results

This paper used four base stations, one tag, and one IMU sensor to conduct positioning tests under stationary and moving states of the mobile platform. The repetitive positioning accuracy of the robotic arm can reach the mm level, which can avoid the jittery situation of the measurement data. Therefore, a KUKA-KR120 robotic arm sited on a 6 m track is selected to represent the mobile platform for this experiment. The UWB tags and IMU modules are fixed on specific robotic arm positions to perform measurements on different trajectories. Different trajectories were set at different heights for the experiments to explore the effect of the height on the positioning results. Subsequently, the corresponding spatial models were built within the Rhinoceros 7 modeling software to obtain the absolute coordinates of each position point on the accurate trajectories. Finally, the experimental results were compared and analyzed with the positional information, and the positioning results were converted into world coordinates recognizable by the robotic arm to apply to mobile intelligent construction scenarios.

#### 4.1. Static Positioning

The robotic arm starts the set operation only when the moving platform is stationary, so stable, high-accuracy positioning is essential when the platform is fixed. At this time, the surrounding environment does not change. Based on this, this paper only analyses the positioning of a single UWB sensor when the mobile platform is stationary.

##### 4.1.1. 2D Positioning Experiment

The experiment was conducted in the Intelligent Construction Laboratory on the ground floor of the Binhai Research Centre of Qingdao University of Technology, in which the UWB base station placement range was set to be a 2D plane of 660 cm  $\times$  700 cm. The uniform height of the base station was 220 cm; the specific placement is shown in Figure 9a. The corresponding base station placement in Rhinoceros is shown in Figure 9b.

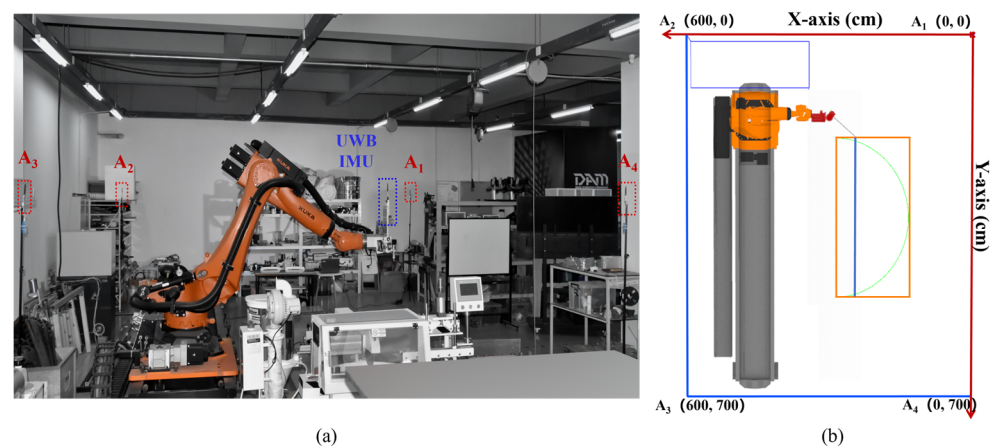


**Figure 9.** Experimental scene. (a) Real scene; (b) Simulation scene.

To study the positioning effect of the mobile platform on the target node in the stationary state, this paper selects eight different fixed position points in the spatial range of UWB erection to conduct 30 positioning tests, respectively, and record the actual position and the estimated position, and the positioning results are shown in Table 1.

**Table 1.** 2D true position vs. estimated position.

Test Point	True Position (cm)	LS Result (cm)	WLS-T Result (cm)
1	(160, 196)	(168.3, 202.1)	(162.0, 196.4)
2	(160, 346)	(166.7, 353.1)	(164.2, 348.9)
3	(160, 496)	(169.4, 503.0)	(162.2, 500.1)
4	(235, 196)	(221.7, 204.3)	(237.2, 198.2)
5	(235, 496)	(244.3, 503.6)	(237.7, 498.4)
6	(310, 196)	(296.8, 202.8)	(304.9, 199.5)
7	(310, 346)	(302.6, 334.5)	(305.1, 343.8)
8	(310, 496)	(300.9, 500.7)	(304.2, 498.3)
Average Error	-	9.6/7.5	3.9/2.7

As can be seen from Table 1, the WLS-T with improved LS algorithm is significantly closer to the actual position compared to the LS algorithm, and the mean value of the positioning accuracy in the x and y directions is improved by 59% and 64%, respectively, compared to the LS algorithm, which improves the target node positioning accuracy.

##### 4.1.2. 3D Positioning Experiment

In order to study the 3D positioning effect of the mobile platform on the target node when it is at rest, in this chapter, the original four base stations are elevated based on the

A4 base station to form a 3D space set to 480 cm  $\times$  600 cm  $\times$  220 cm. The base station placement position is A1 (0, 0, 100), A2 (480, 0, 100), A3 (480, 600, 100), and A4 (0, 600, 320); the actual scene is the same as Figure 9a. According to the working range of the robotic arm, this paper selects six test points with unusual positions in this space to record the actual situation and estimated position, respectively, and the positioning results are shown in Table 2.

**Table 2.** 3D true position vs. estimated position.

Test Point	Ture Position (cm)	LS Result (cm)	WLS-T Result (cm)
1	(185, 170, 200)	(174.6, 161.0, 166.5)	(179.8, 167.1, 187.1)
2	(185, 320, 200)	(175.2, 309.7, 175.3)	(191.1, 312.4, 190.1)
3	(75, 380, 220)	(64.8, 395.3, 199.6)	(66.3, 387.0, 208.4)
4	(225, 380, 220)	(212.1, 364.7, 199.9)	(216.1, 383.2, 207.0)
5	(185, 170, 240)	(171.7, 159.3, 223.6)	(181.3, 165.6, 230.9)
6	(185, 320, 240)	(169.2, 332.7, 216.3)	(176.9, 324.1, 226.2)
Average Error	-	12.1/12.2/23.1	6.7/4.9/11.7

From Table 2, it can be seen that the WLS-T with improved LS algorithm improves in X, Y, and Z direction compared to the LS algorithm, and the mean value of positioning accuracy is improved by 45%, 60%, and 49%, respectively, which improves the positioning effect of the mobile platform as a whole.

#### 4.2. Mobile Positioning

Since the positioning accuracy of a single sensor cannot meet the high-accuracy positioning requirements in mobile scenes, the above IMU sensor is not affected by the outside world. It can only rely on itself to achieve positioning, so this paper adopts the UWB and IMU fusion positioning.

##### 4.2.1. 2D Positioning Experiment

The base station placement position and the preset trajectory are shown in Figure 9. To explore whether the target node under the 2D plane with different heights of base station placement will affect the positioning effect, this paper first designed the positioning experiment of rectangular trajectory under different heights, to judge whether its different heights will affect the positioning results. LS, WLS-T, and ESKF positioning algorithms are also used to determine the positioning effect of the trajectory. The rectangular circuit set for this experiment is 150 cm  $\times$  300 cm, and the positioning experiment is conducted at the height of 210 cm, 220 cm, and 230 cm from the ground, respectively. Figure 10 shows the 2D positioning results of this experiment.

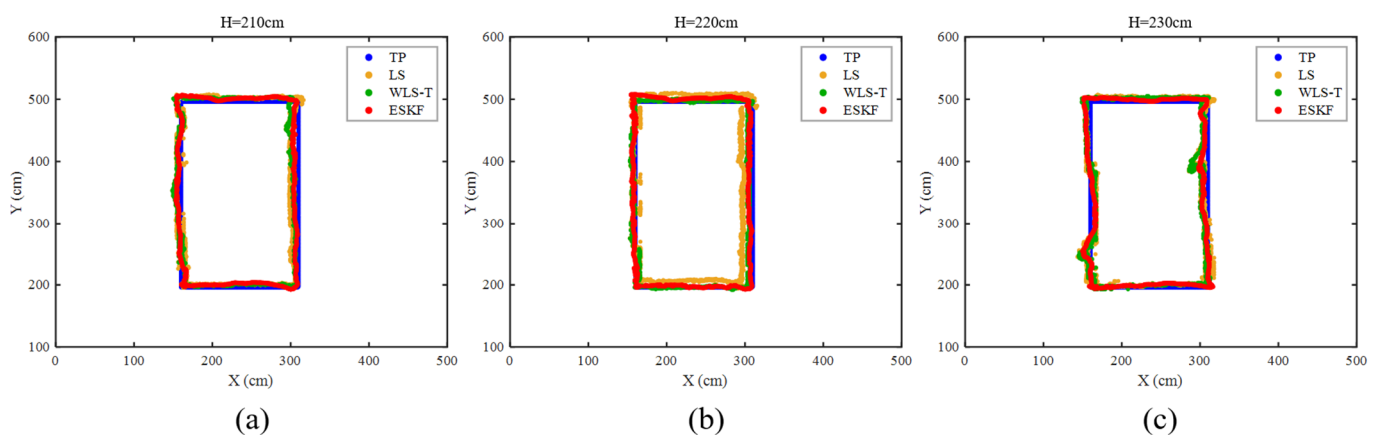


**Figure 10.** Positioning results for rectangles at different heights. (a) H = 210 cm; (b) H = 220 cm; (c) H = 230 cm.

In Figure 10, the blue dots indicate the absolute paths, the orange dots indicate the predicted trajectories obtained from the positioning experiments using the LS algorithm with UWB alone, the green dots show the predicted trajectories obtained from the results obtained by the LS algorithm and the positioning implementations after Taylor convergence, and the red dots indicate the predicted trajectories obtained from the fusion positioning experiments using UWB and IMU. From the positioning results in Figure 10, it can be seen that the LS algorithm's positioning results are dispersive. In contrast, the WLS-T algorithm, after Taylor's optimization, converges the dispersive data of its UWB sensor. Finally, after the fusion of IMU, the ESKF algorithm makes the predicted trajectory closest to the absolute path. When the target node and the base station are at the same height, its ESKF algorithm's prediction result fluctuates less, ensuring positioning accuracy. The error results of the above rectangular positioning can be analyzed in Table 3.

**Table 3.** 2D positioning errors of rectangle at different heights.

	H = 210 cm			H = 220 cm			H = 230 cm		
	LS	WLS-T	ESKF	LS	WLS-T	ESKF	LS	WLS-T	ESKF
X	7.8	6.3	4.9	9.5	6.8	4.0	7.2	6.2	4.8
Y	9.5	8.5	6.8	12	7.8	5.8	9.4	7.1	5.1

From the positioning error data in Table 3, it can be seen that the height of the target node of the mobile platform is not affected by the height of the UWB base station placement when the mobile platform performs 2D positioning. There is no significant difference between the positioning results of each algorithm for rectangles at different heights. In addition, the ESKF fusion positioning algorithm with the addition of IMU reduces the positioning accuracy in the X and Y directions by 44% and 43%, respectively, compared to the LS algorithm which is positioned by UWB only.

Taking the rectangle positioning experiment with a height of 210 cm as an example, the cumulative distribution function (CDF) of positioning error is compared between the fused positioning method and the UWB positioning method alone in the x, y directions, respectively, and the results are shown in Figure 11.

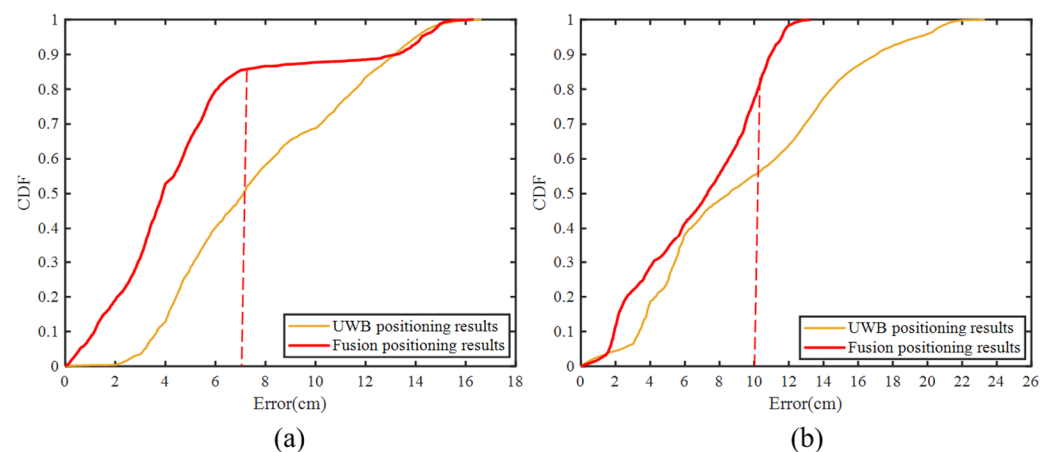


**Figure 11.** CDF comparison diagram of positioning errors of the two positioning methods. (a) Positioning errors in the x-direction. (b) Positioning errors in the y-direction.

According to Figure 11a, it can be seen that the positioning errors of both positioning methods in the X direction are concentrated within 16 cm. About 70% of the point errors are less than 10 cm for positioning by UWB only, while about 85% are less than 7 cm for fused UWB and IMU positioning. Figure 11b shows that when UWB is positioned alone, the error in the Y direction is within 22 cm, and about 80% of the points have an error of

15 cm. The mistake in fused UWB and IMU positioning is within 12 cm, and 80% of the points have an error of 10 cm. It can be seen that the fusion of UWB and IMU significantly improves the positioning accuracy of the trajectory, and most of the positioning errors are less than 10 cm, which can meet the positioning accuracy requirements of this paper.

#### 4.2.2. 3D Positioning Experiment

This paper aims to investigate whether the target node meets the subsequent mobile construction requirements in the height range of [160 cm, 240 cm]. Therefore, two different trajectories, straight and rectangular, are set up in this paper, and experiments are conducted at different heights. In this case, the base station placement is the same as in Section 4.1.2. The LS, WLS-T, and ESKF fusion algorithms estimate their final positioning results and compare them with the true path (TP) to obtain Figure 12. The first column is the projection result of the positioning trajectories of the straight line under different heights on the 2D plane, and the second column is the overall positioning trajectory of the straight line in the 3D space. The third column is the projection error between the measured and actual points in the XOY plane, expressed as the magnitude of  $\vec{a}$ . A vector projection schematic is shown in Figure 13.

As shown in Figure 12, only using the LS algorithm for its positioning, its positioning results are more dispersed, seriously deviating from the actual trajectory. The WLS-T algorithm is more convergent than the LS algorithm, which improves the accuracy of the positioning using only the UWB sensors. Finally, the fusion of UWB and IMU using the ESKF algorithm results in a smoother positioning trajectory. From the third column in Figure 12, the projection on the XOY plane obtained by only the LS algorithm for its positioning has a significant error fluctuation and exceeds 30 cm. In contrast, the projection error on the XOY plane obtained by the Taylor-optimized WLS-T algorithm for its positioning has more than 80% of points within 15 cm, which is a convergence of the UWB positioning results. Finally, after the fusion of the IMU, about 80% of the issues in the ESKF algorithm have an accuracy of 15 cm. The ESKF algorithm has about 80% of the points with an error of 7 cm. The fusion positioning improves the positioning of the trajectory, and the error trajectory is smoother. Finally, the positioning results of the algorithms mentioned above are discussed regarding the average error in each axis direction and the projection error (PE), which is the Euclidean distance between the measured and the actual results in the XOY plane. In this case, the projection distance error on the XOY plane is calculated according to Equation (29), which ultimately leads to the results in Table 4.

$$AE = \frac{1}{i} \sum \sqrt{(x_i - x)^2 + (y_i - y)^2} \quad (29)$$

According to the data in Table 4, it can be seen that the projection vector errors of the measured and actual points on the trajectory after fusion with the ESKF algorithm are all within 10 cm, which satisfies the positioning requirements in the X-Y direction. The positioning errors in the Z direction are all within 15 cm. Compared with single UWB positioning, the ESKF fusion positioning effect has a noticeable improvement. Its vector error in the XOY plane is 6.5 cm on average, while the average PE of the LS algorithm is 12.2 cm and the average PE of the WLS-T algorithm is 8.6 cm, and their mean accuracy values are improved by 47% and 25%, respectively. In the Z direction, the ESKF algorithm improved the mean accuracy value by 47% and 44% compared to the LS and WLS-T algorithms. By analyzing the error results in the X, Y, and Z directions, it can be deduced that the positioning accuracy of the fused ESKF algorithm is significantly improved compared to both the LS algorithm and the WLS-T algorithm.

As shown in Figure 12, the positioning error at the height of 160 cm gradually increases as the trajectory slowly approaches the distance to the highest base station. Meanwhile, the distribution of positioning error at 200 cm and 240 cm elevations is more uniform and without significant fluctuations. Therefore, the height range is further reduced to [200 cm, 240 cm]. To verify the validity of the above height range, this paper adds the rectangular

trajectory at different heights for the positioning experiments on this basis. Figure 14 shows the results of rectangular positioning at different heights.

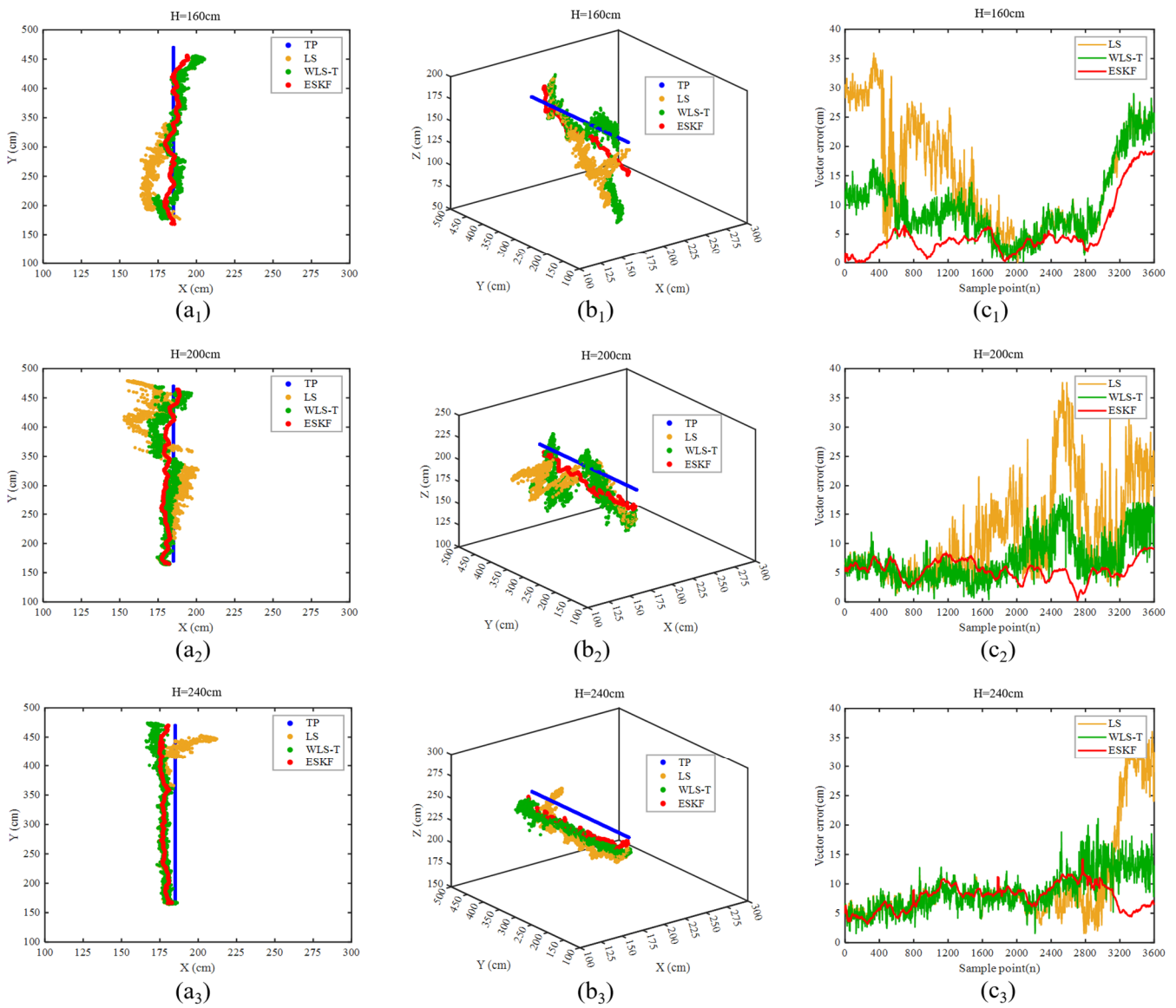


Figure 12. Positioning results of straight lines at different heights. (a<sub>1</sub>–a<sub>3</sub>) XOY plane projection; (b<sub>1</sub>–b<sub>3</sub>) 3D positioning results; (c<sub>1</sub>–c<sub>3</sub>) XOY plane distance error.

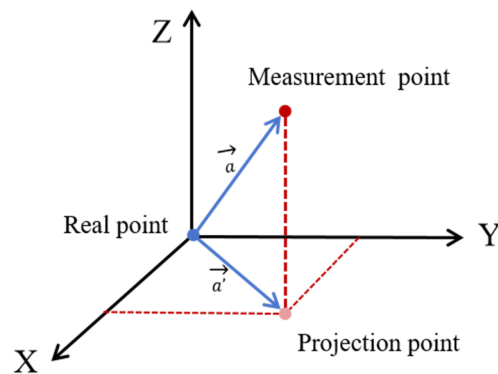
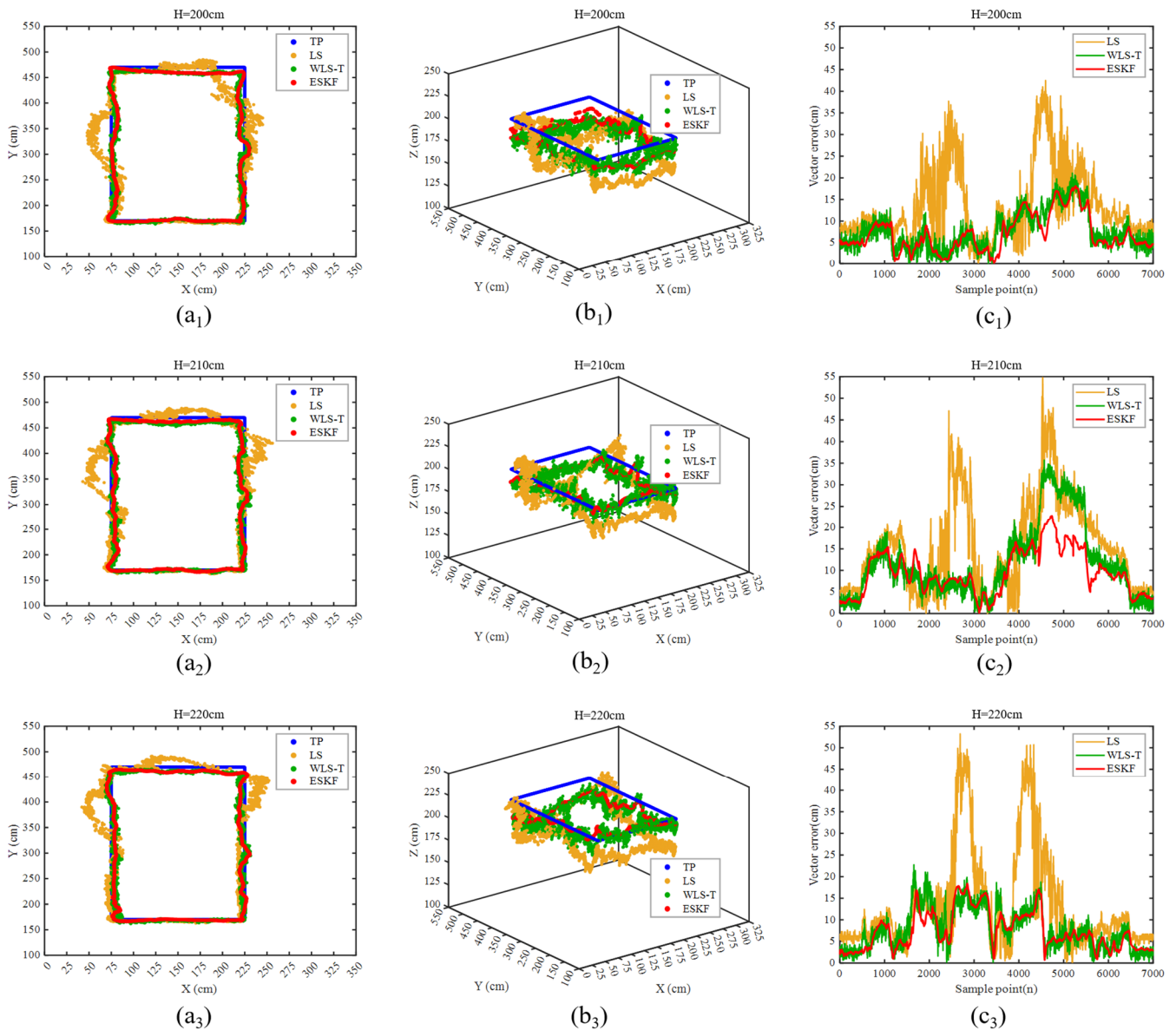


Figure 13. Schematic diagram of a vector projected on the XOY plane.

**Table 4.** Error analysis of straight at different heights and with different positioning algorithms.

	H = 160 cm			H = 200 cm			H = 240 cm		
	LS	WLS-T	ESKF	LS	WLS-T	ESKF	LS	WLS-T	ESKF
X-axis AE	10.2	5.9	4.6	9.1	5.5	4.7	8.2	8.0	6.8
Y-axis AE	10.1	7.4	3.8	6.1	3.9	2.9	4.6	2.7	3.4
Z-axis AE	24.5	20.6	14.2	24.3	23.5	12.9	26.0	24.9	11.7
XOY-PE	14.8	9.9	6.2	11.8	7.3	5.5	10.0	8.7	7.8



**Figure 14.** Positioning results of rectangle at different heights: (a<sub>1</sub>–a<sub>3</sub>) XOY plane projection; (b<sub>1</sub>–b<sub>3</sub>) 3D positioning results; (c<sub>1</sub>–c<sub>3</sub>) XOY plane distance error.

From Figure 14, it can be clearly seen that when the target node is at the corner, the LS algorithm has obvious fluctuation and large error, while the positioning results of the WLS-T positioning algorithm gradually converge to the real trajectory after incorporating the Taylor level. The ESKF algorithm after adding IMU sensors is closer to the real trajectory, and compared with the WLS-T algorithm, its trajectory is smoother and more similar to the real value. The specific analysis of their positioning data can be obtained in Table 5.

**Table 5.** Error analysis of rectangle at different heights and with different positioning algorithms.

	H = 200 cm			H = 210 cm			H = 220 cm		
	LS	WLS-T	ESKF	LS	WLS-T	ESKF	LS	WLS-T	ESKF
X-axis AE	9.3	5.1	4.1	8.8	5.1	5.4	9.3	4.3	4.1
Y-axis AE	8.3	5.4	4.6	10.8	9.1	7.3	8.4	5.8	5.5
Z-axis AE	23.5	16.6	14.5	17.8	8.4	7.1	10.2	9.8	9.5
XOY-PE	13.7	7.6	7.0	15.6	11.7	9.6	13.2	7.9	7.4

As can be seen from Table 5, compared to the LS algorithm, the ESKF algorithm improves the mean value of the accuracy in the XOY plane and Z direction by 44% and 40%, respectively. Its error pattern is consistent with the error pattern in Table 4 above. Therefore, when the height of the target node is in the range of [200 cm, 240 cm], it can meet the experimental requirements of this paper.

#### 4.3. Experimental Validation

Since the experimental site of this study only involves position transformation in the X and Y direction, the KUKA-KR60 robotic arm with a tracked chassis is used as the MCP for the experiments in this paper, and the 2D plane is used as an example to verify the positioning effect of the above method in the stationary and moving states of the MCP, as shown in Figure 15.

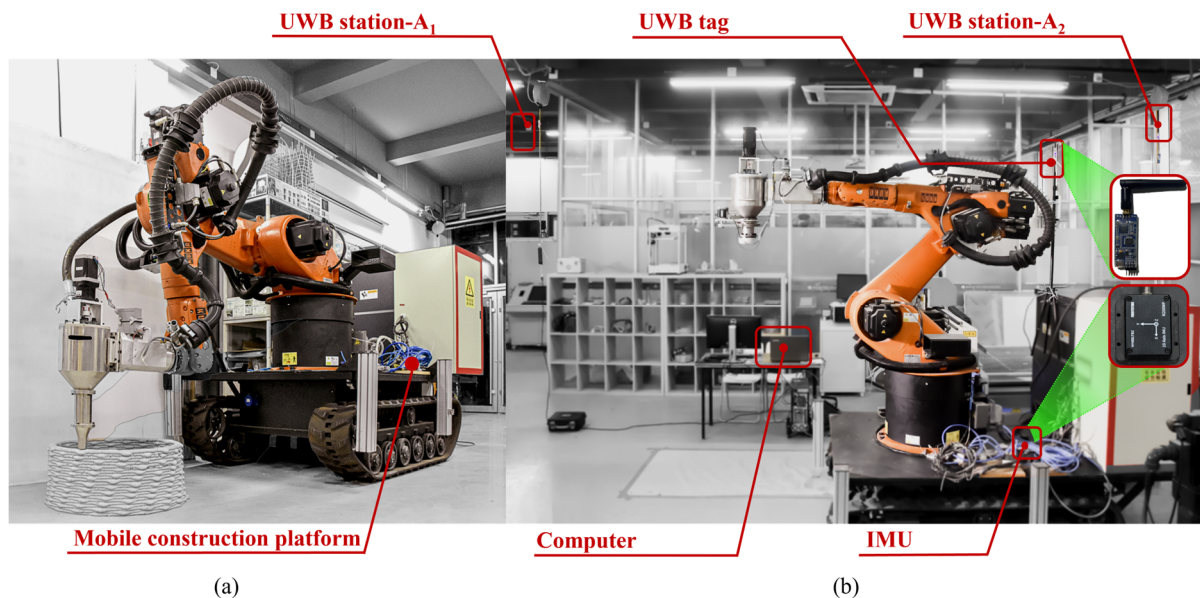


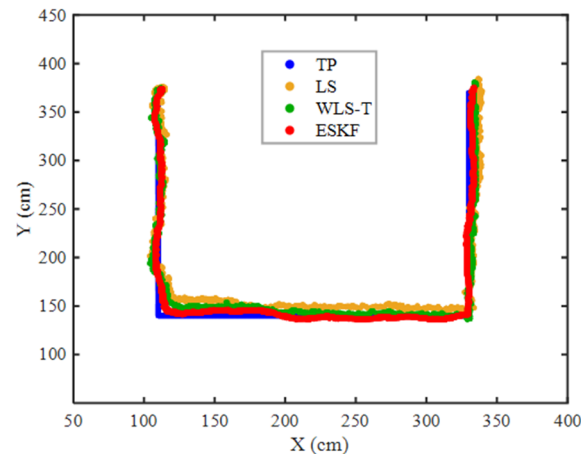
**Figure 15.** Experimental validation of positioning in real experimental scenarios: (a) MCP; (b) installation position of each sensor.

When the MCP was stationary, 6 positioning points were selected for fixation tests, and each position point was tested for 200 positioning tests, respectively. The data analysis of the positioning results of these 6 test points leads to Table 6.

Due to the limitations of the experimental site and the size of the KUKA-KR60 MCP, this paper verifies the positioning effect of the platform in the mobile state by controlling the MCP to take a “U” shaped trajectory in the real site. The positioning results are shown in Figure 16.

**Table 6.** Analysis of positioning results for stationary point positions.

Test Point	True Position (cm)	LS Result (cm)	WLS-T Result (cm)
1	(300, 505)	(295.1, 511.1)	(303.8, 509.8)
2	(260, 230)	(256.3, 223.9)	(256.8, 226.3)
3	(400, 490)	(405.2, 483.4)	(402.1, 493.2)
4	(221, 60)	(215.6, 67.4)	(222.4, 56.7)
5	(360, 35)	(366.4, 42.6)	(361.4, 37.4)
6	(207, 525)	(201.1, 532.4)	(204.7, 527.7)
Average Error	-	5.3/6.9	2.4/3.6

**Figure 16.** Positioning results for “U” shaped trajectory.

From Table 6 and Figure 16, it can be seen that when the MCP is in a stationary state, the improved WLS-T algorithm’s positioning results for fixed position points are closer to the true position compared to the LS algorithm. When the MCP is in motion, the trajectory of the improved ESKF algorithm with IMU fusion is closer to the real path than the LS and WLS-T algorithms with UWB sensors only, and the positioning points on the trajectory converge near the real trajectory. The error analysis of the positioning results of this “U” shaped trajectory is shown in Table 7.

**Table 7.** Positioning error analysis of U-shaped trajectory.

Error	LS (cm)	WLS-T (cm)	ESKF (cm)
X	8.7	7.0	3.9
Y	9.1	6.7	5.2
XOY-PE	16.1	12.8	8.0

As can be seen from Tables 6 and 7, when the MCP is in a stationary state, the positioning results of the improved WLS-T algorithm for fixed position points are closer to the real position compared to the LS algorithm. When the mobile platform is in motion, the trajectory of the ESKF algorithm with fused IMU is closer to the TP and the positioning points on the trajectory converge nearer the true trajectory compared to the LS and WLS-T algorithms that only use UWB sensors. By fusing the preprocessed raw UWB data with the data from the IMU using the ESKF algorithm, the mean absolute error in the X and Y directions is 4.5 cm. In summary, the results validate the effectiveness of the above method and demonstrate that the method proposed in this paper can be used for the positioning of mobile platforms in real scenarios.

## 5. Construction Simulation

### 5.1. Simulation Experiment Process

In order to realize the continuous simulation construction of the MCP, it is necessary to know the specific position of the platform at the current moment, and then combine the construction position with the simulation construction operation of the robotic arm. Figure 17 introduces the simulation construction experimental process of this paper.

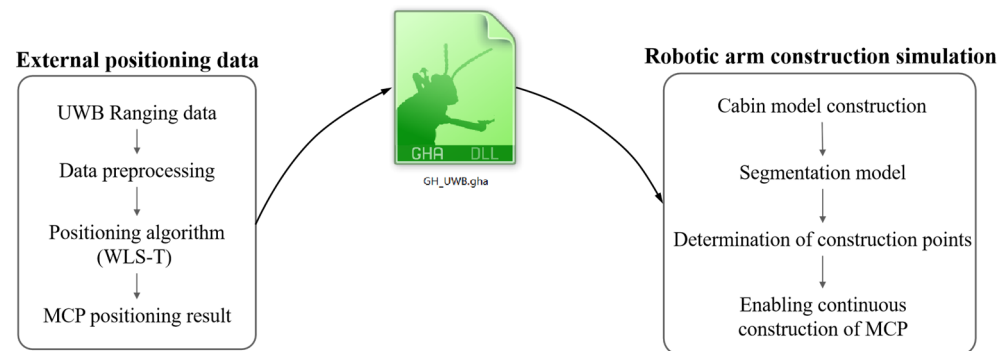


**Figure 17.** MCP construction simulation process.

As can be seen from Figure 17, it is necessary to output the positioning data through the external positioning sensors and preprocess them to eliminate the ranging error and improve the positioning accuracy. In this paper, the above improved high-accuracy positioning algorithm is written as a GH block in the WLS-T algorithm, and the coordinate system conversion is performed on the positioning result to convert the positioning information into the position information of the platform in Rhinoceros.

Since the large-scale building model cannot be built directly by the existing robotic arm in one go, this experiment prepares the model separately according to the slice position of the above model, and the initial building position of the MCP is shown in Figure 18. In this paper, the KUKA-KR60 MCP equipped with a chassis and lift is used to create simulation construction experiments for large-scale models. The construction planes were extracted from the center spot of the tested block placement planes, and the construction planes were inputted into the KUKA | prc core operator, which automatically produces KUKA Motion Command to control the movement of the robotic arm.

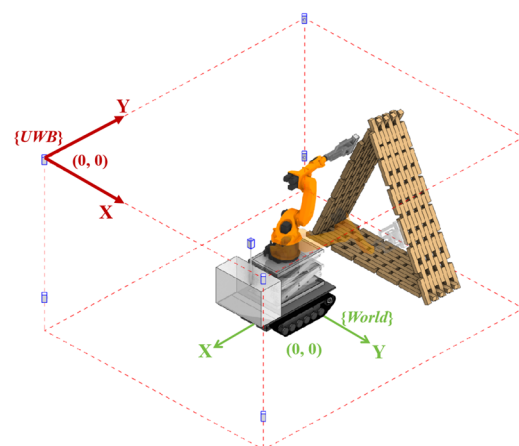


**Figure 18.** Initial construction position of MCP.

For subsequent mobile intelligent construction design research, it is crucial to accurately obtain the positional information of the robotic arm to facilitate the completion of the corresponding operation of the robotic arm. Since the mobile robot starts to perform

the related operations only when it is at stationary mode, this paper adopts the C# language to custom-definition the GH plug-in, which implements the real-time transmission of the previously optimized UWB positioning results into Rhinoceros and converts the {UWB} coordinate system into the {World} coordinate system through the coordinate system conversion to obtain the position information of the robotic arm under the {World} coordinate system.

See Figure 18 for an example of a transformation relationship between two coordinate systems established in Rhinoceros, from which the relationship between the new coordinates and the original coordinates can be obtained.

$$\begin{bmatrix} x \\ y \end{bmatrix} = \begin{bmatrix} 460 \\ 600 \end{bmatrix} + \begin{bmatrix} \cos \theta & -\sin \theta \\ \sin \theta & \cos \theta \end{bmatrix} \begin{bmatrix} x \\ y \end{bmatrix} = \begin{bmatrix} 460 - x \\ 600 - y \end{bmatrix} \quad (30)$$

According to the conversion relationship of the coordinate system mentioned above, the GH plug-in block after completing the coordinate conversion is shown in Figure 19. Component A is the positioning module, which is used to transfer the external positioning information into Rhinoceros in real-time. Component B is the coordinate conversion module, which is used to convert the positioning data in this paper to the positioning data under the {World} coordinate system.

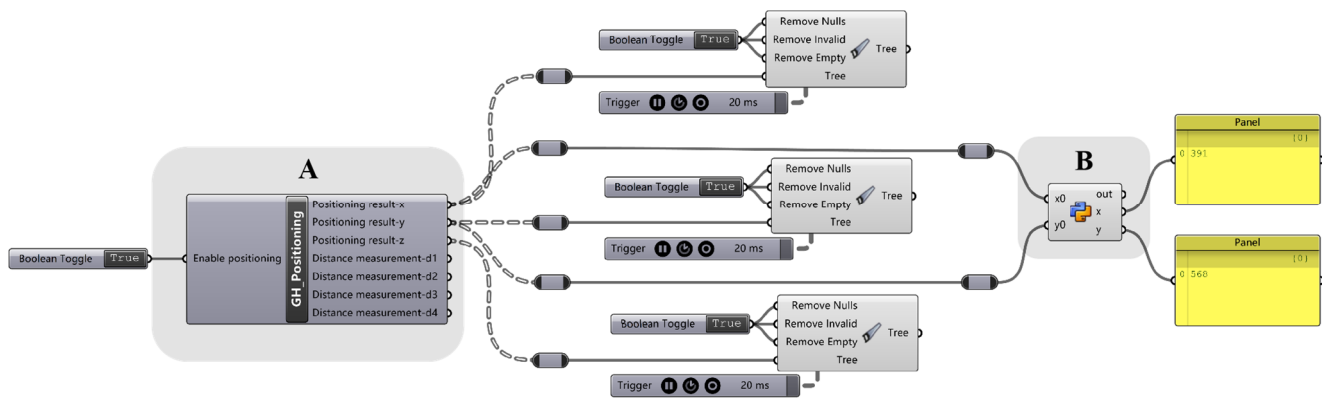


**Figure 19.** Realization of robotic arm positioning conversion diagrams.

## 5.2. Application of Construction Simulation for Wooden-Cabin

### 5.2.1. Cabin Model

In this paper, a large-scale model is prepared based on Rhinoceros modeling software and visual programming plug-in GH, and KUKA | prc is used to prepare the motion path for the simulation model based on robotic arm.

In order to apply the above method to a real construction scenario, a large-scale model of a cabin, for example, was built, as shown in Figure 20. The model has a base of 330 cm × 400 cm and a height of 420 cm. The whole wooden construction model consists of wood blocks with a uniform size of 60 cm × 10.5 cm × 10.5 cm, totaling 737 blocks. The MCP is only responsible for vertically constructing the main A, B, and C parts of the cabin model, with a total of 30 layers and 536 wooden blocks, while the front and rear parts of the model are pre-constructed. As the working range of the KUKA-KR60 is within 210 cm, it is not possible to realize a complete construction within a fixed working range, so it is necessary to equip it with a mobile chassis to complete the overall construction process. The system is not always in the same position during the entire construction process, but builds, moves, and builds again, cyclically, by changing the construction position of the mobile platform to complete the construction of large-scale models. According to the working range of the KUKA-KR60 arm and the size of the target model, the model is separated into 3 parts and built sequentially, and all of the wooden blocks are built according to the preconfigured path during the whole building process.

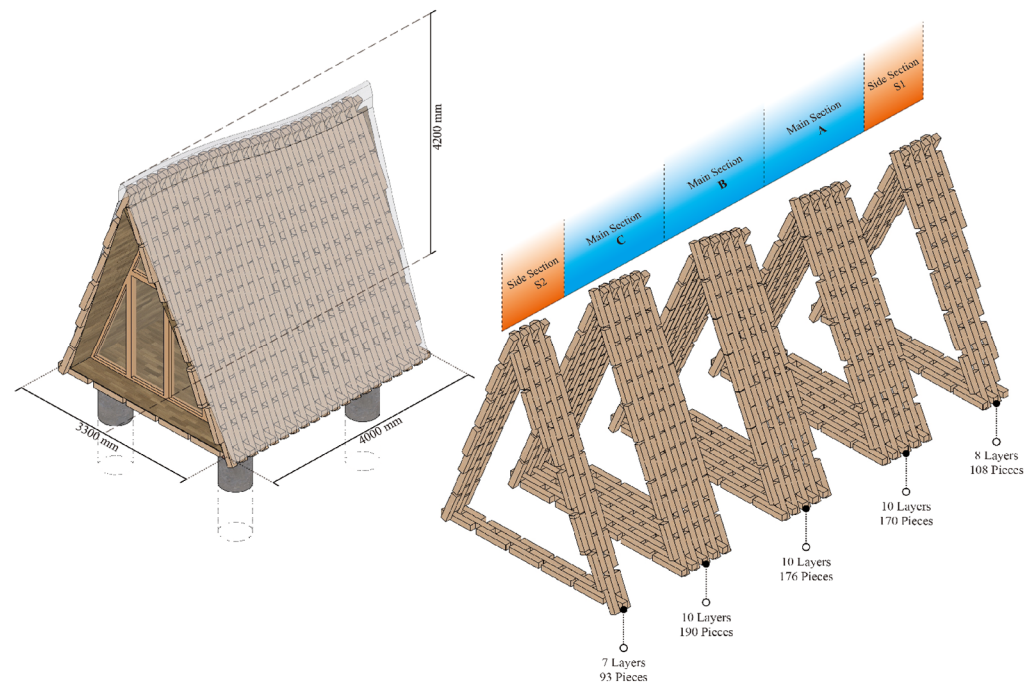


**Figure 20.** Cabin model for robotic construction with MCP.

During the construction process, the change in the position of the MCP results in a change in the relative position of this robotic arm to the target component. It is therefore necessary to associate the position of the mobile platform after it has been moved with the position of the successive construction. In this paper, the complete construction of this workflow is achieved by integrating the mentioned positioning plug-in module with the process of continuously mobile construction of the wooden structure model.

### 5.2.2. Continuous Construction Simulation

When the first part of the construction is completed, the MCP needs to move to the second task spot for the second part of the construction, as shown in Figure 21a. The position and sequence of the second part of the wooden model constructed by the MCP is shown in Figure 21b. In this case, the construction sequence is the same for each section of the model.

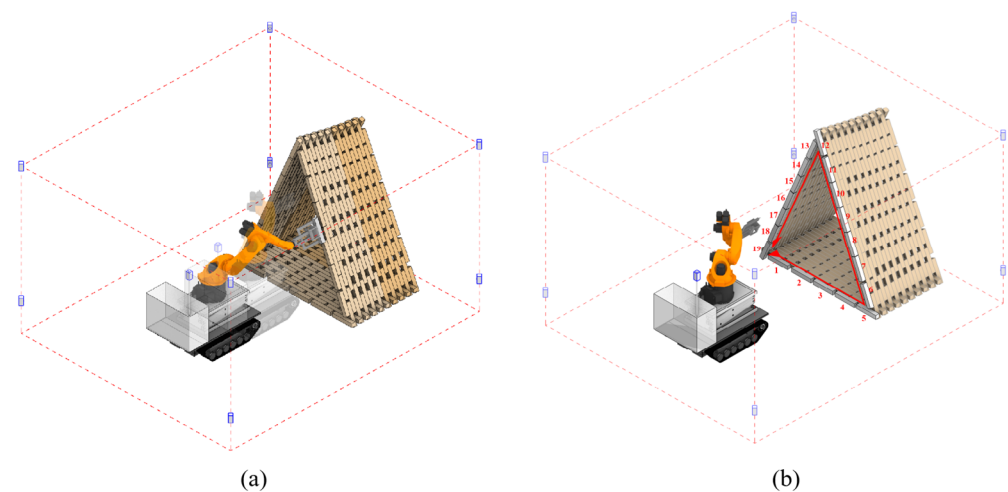


**Figure 21.** MCP construction process. (a) MCP at Main Section B. (b) Sequence of wooden frame construction on each layer.

In the KUKA |prc plug-in of GH, it is not possible to change the position of the MCP directly from external data. Therefore, in this paper, the position of the platform within Rhinoceros is changed by changing the position of the construction plane of the robotic arm and then the position of the platform through the inverse kinematics of the robotic arm, thus realizing the continuous simulation building operation of the MCP. The entire mobile simulation of the GH definition component is shown in Figure 22a. The final vertically constructed cabin model of the MCP is shown in Figure 22b.

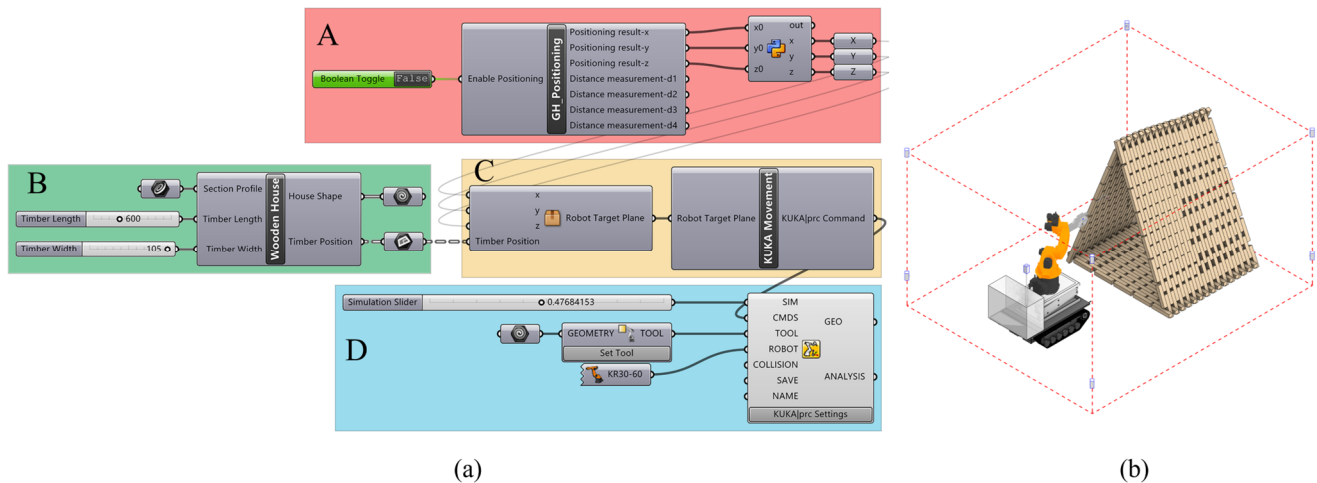


**Figure 22.** Continuous simulation construction realization process. (a) Simulation construction process. (b) Complete large-scale model.

In this case, the procedure to build the wooden model of the simulation is divided into four parts. The first part of the GH definition (A in Figure 22a) is responsible for transferring the position information of the platform in the external {UWB} coordinate system to the GH platform, and then calculating the position relationship between the two coordinate systems based on the {UWB} coordinate system and the {World} world coordinate system in the real scene, which is then transformed into the world coordinates available for the robotic arm. The second part (B) is based on the Rhinoceros modelling software to create the overall model of the cabin, in which the size of the wooden blocks is adjustable, so that the shape of the main structure of the cabin can be adjusted at any time. The third part (C) is responsible for the positioning value of the coupling platform and the plane of the wooden block construction, by changing the building position of the wooden block at the next task point, thus realizing the whole continuous construction workflow. The fourth part (D) is the simulation operation part, which can manually adjust the value of the SIM slider to view the simulated building process of the platform at the current position. At this point, the continuous on-site construction simulation experiment has been completed.

As a result, the on-site continuous construction simulation experiment of the MCP realized in this paper proves that the combination of the mobile construction platform's positioning technique and robotic construction technique can provide the feasibility of realizing on-site large-scale construction in the future. Since the positioning algorithm proposed in this paper shows high accuracy in the set placement range of UWB base station of  $600 \text{ cm} \times 700 \text{ cm}$ , the positioning technique investigated in this paper is applicable to any on-site large-scale building construction within this range.

## 6. Conclusions

In the mobile intelligent construction process, the reliable positioning technology of the MCP is critical. This paper conducts the positioning experiments for MCPs in two different states, stationary and moving, when it performs the construction work. A KUKA-KR120

carrying UWB tags and IMU sensors are used for the positioning test. The experimental results show that in the stationary state, when only the UWB sensor is used for positioning, the improved WLS-T algorithm improves the positioning accuracy by 53% on average compared with the LS algorithm. In the moving state, using fused positioning with UWB and IMU sensors, the ESKF fused positioning algorithm improves the positioning accuracy in the XOY plane and Z direction by 46% on average compared to the LS algorithm. When the method is ported to a real KUKA-KR60 MCP, the static positioning errors in the X and Y directions are 2.4 cm and 3.6 cm, respectively. In the mobile state, the positioning errors in the x and y directions are 3.9 cm and 5.2 cm, and the trajectory error is 8 cm. Compared with other studies, which have errors of 4.1 cm and 5.8 cm in the x and y directions [58], and trajectory errors of 28 cm and 10 cm [60,61], the method in this paper shows a high level of positioning accuracy.

In this paper, the above positioning results are verified using a KUKA-KR60 MCP equipped with chassis for positioning verification. A custom GH plug-in is programmed using C#, which can transmit the positioning results in the stationary state to the Rhinoceros modeling software in real-time, and finally carry out the conversion to the position information in the {world} coordinate system that can be recognized by the robotic arm, in order to correspond to the position of the subsequent operation. In order to better apply the positioning technology in the field of mobile construction, this paper finally integrates the above positioning plug-in in a large-scale model and realizes on-site continuous simulation construction by positioning the MCP with the real-time positioning data, which confirms the effectiveness of the method proposed in this paper. However, there are still some shortcomings, as well as directions in which improvements can be made. (1) In this paper, only four UWB base stations are used in 3D space, and there is still some error in the non-line-of-sight situation; therefore, more base stations can be added in the future to make the positioning more accurate. (2) In the stationary state, only the UWB positioning algorithm is improved, and it can be fused with more sensors in the future to better improve the positioning accuracy and increase the stability of the system. (3) The positioning algorithm in the mobile state and the positioning algorithm in the stationary state cannot be switched in real time, and in the future, it can be designed as a seamless switching algorithm operation to reduce the operation time of the whole construction process. (4) This study is limited by the surrounding environment; the simulated environment was constructed to ensure that there is no obstruction between the UWB base stations, the dimension of wood component is unified, and the operation height of the MCP is limited, all of which could be improved in future studies.

In order to meet the needs of mobile construction in real scenarios, it is necessary to combine the positioning results with the operation of the robotic arm and to consider more influencing factors in the construction environment, so as to better realize the continuous on-site construction tasks.

**Author Contributions:** Conceptualization, X.S. and D.W.; methodology, X.S., C.W., T.K.P. and D.W.; software, C.W. and C.S.; validation, C.W., H.Z. and W.Z.; resources, X.S.; writing—original draft preparation, C.W.; writing—review and editing, X.S., T.K.P. and D.W.; visualization, C.S. and W.Z.; supervision, W.C. and D.W.; project administration, X.S.; funding acquisition, X.S. All authors have read and agreed to the published version of the manuscript.

**Funding:** This research was funded by (the department of Education of Shandong Province—Youth Tutor Visting and Training Project), (the Key Technology Research and Development Program of Shandong) grant number (2019GSF110004), and (the research program of National Natural Science Foundation of China Youth Science Fund Project) grant number (52008224).

**Data Availability Statement:** The data presented in this study are available upon request from the corresponding author.

**Acknowledgments:** We are very grateful to Meng Wang and Liang Shen (DAMlab, Qingdao University of Technology), Kang Bi (Faculty of Environmental Engineering, The University of Kitakyushu, Japan) for their generous advice and help in the research process, as well as the DAMlab (Digital Architecture and Manufacture Laboratory) in Qingdao University of Technology for providing highly qualified equipment support during this study.

**Conflicts of Interest:** Tyson Keen Phillips was employed by the company Piaggio Fast Forward Co., Ltd. The remaining authors declare that the research was conducted in the absence of any commercial or financial relationships that could be construed as a potential conflict of interest.

## References

- Kramberger, A.; Kunic, A.; Iturrate, I.; Sloth, C.; Naboni, R.; Schlette, C. Robotic Assembly of Timber Structures in a Human-Robot Collaboration Setup. *Front. Robot. AI* **2022**, *8*, 768038. [[CrossRef](#)] [[PubMed](#)]
- Chong, O.W.; Zhang, J.; Voyles, R.M.; Min, B.-C. BIM-based simulation of construction robotics in the assembly process of wood frames. *Autom. Constr.* **2022**, *137*, 104194. [[CrossRef](#)]
- Jenny, S.E.; Pietrasik, L.L.; Sounigo, E.; Tsai, P.-H.; Gramazio, F.; Kohler, M.; Lloret-Fritsch, E.; Hutter, M. Continuous Mobile Thin-Layer On-Site Printing. *Autom. Constr.* **2023**, *146*, 104634. [[CrossRef](#)]
- Hercik, R.; Byrtus, R.; Jaros, R.; Koziorek, J. Implementation of Autonomous Mobile Robot in SmartFactory. *Appl. Sci.* **2022**, *12*, 8912. [[CrossRef](#)]
- Babinec, A.; Jurišica, L.; Hubinský, P.; Duchoň, F. Visual Localization of Mobile Robot Using Artificial Markers. *Procedia Eng.* **2014**, *96*, 1–9. [[CrossRef](#)]
- Belkin, I.; Abramenko, A.; Yudin, D. Real-Time Lidar-based Localization of Mobile Ground Robot. *Procedia Comput. Sci.* **2021**, *186*, 440–448. [[CrossRef](#)]
- Mikulová, Z.; Duchoň, F.; Dekan, M.; Babinec, A. Localization of mobile robot using visual system. *Int. J. Adv. Robot. Syst.* **2017**, *14*, 1729881417736085. [[CrossRef](#)]
- Huang, J.; Junginger, S.; Liu, H.; Thurow, K. Indoor Positioning Systems of Mobile Robots: A Review. *Robotics* **2023**, *12*, 47. [[CrossRef](#)]
- Loganathan, A.; Ahmad, N.S. A systematic review on recent advances in autonomous mobile robot navigation. *Eng. Sci. Technol. Int. J.* **2023**, *40*, 101343. [[CrossRef](#)]
- Sandy, T.; Gifftaler, M.; Dörfler, K.; Kohler, M.; Buchli, J. Autonomous repositioning and localization of an in situ fabricator. In Proceedings of the 2016 IEEE International Conference on Robotics and Automation (ICRA), Stockholm, Sweden, 16–21 May 2016; IEEE: Piscataway, NJ, USA, 2016; pp. 2852–2858. [[CrossRef](#)]
- Zeng, L.; Guo, S.; Zhu, M.; Duan, H.; Bai, J. An Improved Trilateral Localization Technique Fusing Extended Kalman Filter for Mobile Construction Robot. *Buildings* **2024**, *14*, 1026. [[CrossRef](#)]
- Kim, J.; Kim, Y.; Kim, S. An accurate localization for mobile robot using extended Kalman filter and sensor fusion. In Proceedings of the 2008 IEEE International Joint Conference on Neural Networks (IEEE World Congress on Computational Intelligence), Hong Kong, China, 1–6 June 2008; IEEE: Piscataway, NJ, USA, 2008; pp. 2928–2933. [[CrossRef](#)]
- Guosheng, W.; Shuqi, Q.; Qiang, L.; Heng, W.; Huican, L.; Bing, L. UWB and IMU system fusion for indoor navigation. In Proceedings of the 2018 37th Chinese Control Conference (CCC), Wuhan, China, 25–27 July 2018; IEEE: Piscataway, NJ, USA, 2018; pp. 4946–4950. [[CrossRef](#)]
- Gao, Y.; Wang, F.; Li, J.; Liu, Y. Localization of mobile robot based on multi-sensor fusion. In Proceedings of the 2020 Chinese Control and Decision Conference (CCDC), Hefei, China, 22–24 August 2020; IEEE: Piscataway, NJ, USA, 2020; pp. 4367–4372. [[CrossRef](#)]
- Möller, C.; Schmidt, H.C.; Koch, P.; Böhlmann, C.; Kothe, S.-M.; Wollnack, J.; Hintze, W. Machining of large scaled CFRP-Parts with mobile CNC-based robotic system in aerospace industry. *Procedia Manuf.* **2017**, *14*, 17–29. [[CrossRef](#)]
- Parikh, P.; Kalamdane, S.; Rasal, A.; Mundada, K.; Kalshetti, U. Spark-bot: An educational robotic platform. In Proceedings of the 2022 IEEE Global Engineering Education Conference (EDUCON), Tunis, Tunisia, 28–31 March 2022; IEEE: Piscataway, NJ, USA, 2022; pp. 1628–1633. [[CrossRef](#)]
- Chu, B.; Jung, K.; Lim, M.-T.; Hong, D. Robot-based construction automation: An application to steel beam assembly (Part I). *Autom. Constr.* **2013**, *32*, 46–61. [[CrossRef](#)]
- Melenbrink, N.; Werfel, J.; Menges, A. On-site autonomous construction robots: Towards unsupervised building. *Autom. Constr.* **2020**, *119*, 103312. [[CrossRef](#)]
- Tao, B.; Zhao, X.; Ding, H. Mobile-robotic machining for large complex components: A review study. *Sci. China Technol. Sci.* **2019**, *62*, 1388–1400. [[CrossRef](#)]
- Helm, V.; Willmann, J.; Gramazio, F.; Kohler, M. In-situ robotic fabrication: Advanced digital manufacturing beyond the laboratory. In *Gearing Up and Accelerating Cross-Fertilization between Academic and Industrial Robotics Research in Europe: Technology Transfer Experiments from the ECHORD Project*; Springer International Publishing: Berlin/Heidelberg, Germany, 2014; pp. 63–83. [[CrossRef](#)]
- Khatib, O.; Yokoi, K.; Brock, O.; Chang, K.; Casal, A. Robots in Human Environments: Basic Autonomous Capabilities. *Int. J. Robot. Res.* **1999**, *18*, 684–696. [[CrossRef](#)]

22. Helms, E.; Schraft, R.D.; Hagele, M. rob@ work: Robot assistant in industrial environments. In Proceedings of the 11th IEEE International Workshop on Robot and Human Interactive Communication, Shenzhen, China, 13–14 November 2002; IEEE: Piscataway, NJ, USA, 2002; pp. 399–404. [\[CrossRef\]](#)
23. Asfour, T.; Berns, K.; Dillmann, R. The humanoid robot ARMAR: Design and control. In Proceedings of the 1st IEEE-ras International Conference on Humanoid Robots (Humanoids 2000), Cambridge, MA, USA, 7 September 2000; pp. 7–8.
24. Schuler, J. *Integration von Förder-und Handhabungseinrichtungen*; Springer: Berlin/Heidelberg, Germany, 2013.
25. Yamamoto, Y.; Yun, X. Effect of the dynamic interaction on coordinated control of mobile manipulators. *IEEE Trans. Robot. Autom.* **1996**, *12*, 816–824. [\[CrossRef\]](#)
26. Norman, A.R.; Schönberg, A.; Gorchach, I.A.; Schmitt, R. Validation of iGPS as an external measurement system for cooperative robot positioning. *Int. J. Adv. Manuf. Technol.* **2012**, *64*, 427–446. [\[CrossRef\]](#)
27. Jiang, Z.-H. Workspace trajectory control of flexible robot manipulators using neural network and visual sensor feedback. In Proceedings of the 2015 IEEE 28th Canadian Conference on Electrical and Computer Engineering (CCECE), Halifax, NS, Canada, 3–6 May 2015; IEEE: Piscataway, NJ, USA, 2015; pp. 1502–1507. [\[CrossRef\]](#)
28. Susemihl, H.; Moeller, C.; Kothe, S.; Schmidt, H.C.; Shah, N.; Brillinger, C.; Wollnack, J.; Hintze, W. High Accuracy Mobile Robotic System for Machining of Large Aircraft Components. *SAE Int. J. Aerosp.* **2016**, *9*, 231–238. [\[CrossRef\]](#)
29. Helm, V.; Ercan, S.; Gramazio, F.; Kohler, M. Mobile robotic fabrication on construction sites: DimRob. In Proceedings of the 2012 IEEE/RSJ International Conference on Intelligent Robots and Systems, Vilamoura-Algarve, Portugal, 7–12 October 2012; IEEE: Piscataway, NJ, USA, 2012; pp. 4335–4341. [\[CrossRef\]](#)
30. Dörfler, K.; Sandy, T.; Gifftthaler, M.; Gramazio, F.; Kohler, M.; Buchli, J. Mobile robotic brickwork: Automation of a discrete robotic fabrication process using an autonomous mobile robot. In *Robotic Fabrication in Architecture, Art and Design 2016*; Springer: Berlin/Heidelberg, Germany, 2016; pp. 204–217. [\[CrossRef\]](#)
31. Lussi, M.; Sandy, T.; Dorfler, K.; Hack, N.; Gramazio, F.; Kohler, M.; Buchli, J. Accurate and adaptive in situ fabrication of an undulated wall using an on-board visual sensing system. In Proceedings of the 2018 IEEE International Conference on Robotics and Automation (ICRA), Brisbane, Australia, 21–25 May 2018; IEEE: Piscataway, NJ, USA, 2018; pp. 3532–3539. [\[CrossRef\]](#)
32. Gawel, A.; Siegwart, R.; Hutter, M.; Sandy, T.; Blum, H.; Pankert, J.; Kramer, K.; Bartolomei, L.; Ercan, S.; Farshidian, F.; et al. A fully-integrated sensing and control system for high-accuracy mobile robotic building construction. In Proceedings of the 2019 IEEE/RSJ International Conference on Intelligent Robots and Systems (IROS), Macau, China, 3–8 November 2019; IEEE: Piscataway, NJ, USA, 2019; pp. 2300–2307. [\[CrossRef\]](#)
33. Hamner, B.; Koterba, S.; Shi, J.; Simmons, R.; Singh, S. An autonomous mobile manipulator for assembly tasks. *Auton. Robot.* **2009**, *28*, 131–149. [\[CrossRef\]](#)
34. Chai, H.; Wagner, H.J.; Guo, Z.; Qi, Y.; Menges, A.; Yuan, P.F. Computational design and on-site mobile robotic construction of an adaptive reinforcement beam network for cross-laminated timber slab panels. *Autom. Constr.* **2022**, *142*, 104536. [\[CrossRef\]](#)
35. Wang, L.; Naito, T.; Leng, Y.; Fukuda, H.; Zhang, T. Research on Construction Performance Evaluation of Robot in Wooden Structure Building Method. *Buildings* **2022**, *12*, 1437. [\[CrossRef\]](#)
36. Zhao, S.; Huang, B.; Liu, F. Localization of Indoor Mobile Robot Using Minimum Variance Unbiased FIR Filter. *IEEE Trans. Autom. Sci. Eng.* **2016**, *15*, 410–419. [\[CrossRef\]](#)
37. Semborski, J.; Idzkowski, A. A review on positioning techniques of mobile robots. *Robot. Syst. Appl.* **2024**, *4*. [\[CrossRef\]](#)
38. Gentner, C.; Ulmschneider, M.; Kuehner, I.; Dammann, A. WiFi-RTT indoor positioning. In Proceedings of the 2020 IEEE/ION Position, Location and Navigation Symposium (PLANS), Portland, OR, USA, 20–23 April 2020; IEEE: Piscataway, NJ, USA, 2020; pp. 1029–1035. [\[CrossRef\]](#)
39. Xu, D.; Han, L.; Tan, M.; Li, Y.F. Ceiling-Based Visual Positioning for an Indoor Mobile Robot with Monocular Vision. *IEEE Trans. Ind. Electron.* **2009**, *56*, 1617–1628. [\[CrossRef\]](#)
40. Jung, M.; Song, J.-B. Robust mapping and localization in indoor environments. *Intell. Serv. Robot.* **2016**, *10*, 55–66. [\[CrossRef\]](#)
41. Dardari, D.; Conti, A.; Ferner, U.; Giorgetti, A.; Win, M.Z. Ranging with Ultrawide Bandwidth Signals in Multipath Environments. *Proc. IEEE* **2009**, *97*, 404–426. [\[CrossRef\]](#)
42. Richardson, P.; Shan, D. Experimental Data Collection and Performance Analysis of Outdoor UWB Positioning System under Static and Mobile Conditions. *EURASIP J. Wirel. Commun. Netw.* **2010**, *2009*, 618036. [\[CrossRef\]](#)
43. Li, B.; Zhao, K.; Sandoval, E.B. A UWB-Based Indoor Positioning System Employing Neural Networks. *J. Geovisualization Spat. Anal.* **2020**, *4*, 18. [\[CrossRef\]](#)
44. Takahara, H.; Ohno, K.; Itami, M. A study on UWB radar assisted by inter-vehicle communication for safety applications. In Proceedings of the 2012 IEEE International Conference on Vehicular Electronics and Safety (ICVES 2012), Istanbul, Turkey, 24–27 July 2012; IEEE: Piscataway, NJ, USA, 2012; pp. 99–104. [\[CrossRef\]](#)
45. Ershadh, M. Study of the design evolution of an antenna and its performance for UWB communications. *Microw. Opt. Technol. Lett.* **2014**, *57*, 81–84. [\[CrossRef\]](#)
46. Yang, K.; Liu, M.; Xie, Y.; Zhang, X.; Wang, W.; Gou, S.; Su, H. Research on UWB/IMU location fusion algorithm based on GA-BP neural network. In Proceedings of the 2021 40th Chinese Control Conference (CCC), Shanghai, China, 26–28 July 2021; IEEE: Piscataway, NJ, USA, 2021; pp. 8111–8116. [\[CrossRef\]](#)
47. Kalman, R.E. A new approach to linear filtering and prediction problems. *J. Basic Eng.* **1960**, *82*, 35–45. [\[CrossRef\]](#)

48. Konatowski, S.; Kaniewski, P.; Matuszewski, J. Comparison of Estimation Accuracy of EKF, UKF and PF Filters. *Annu. Navig.* **2016**, *23*, 69–87. [[CrossRef](#)]
49. Li, M.; Mourikis, A.I. High-precision, consistent EKF-based visual-inertial odometry. *Int. J. Robot. Res.* **2013**, *32*, 690–711. [[CrossRef](#)]
50. Julier, S.; Uhlmann, J.; Durrant-Whyte, H.F. A new method for the nonlinear transformation of means and covariances in filters and estimators. *IEEE Trans. Autom. Control* **2001**, *45*, 477–482. [[CrossRef](#)]
51. Arasaratnam, I.; Haykin, S. Cubature kalman filters. *IEEE Trans. Autom. Control.* **2009**, *54*, 1254–1269. [[CrossRef](#)]
52. Lee, W.; Chung, W. Position estimation using multiple low-cost GPS receivers for outdoor mobile robots. In Proceedings of the 2015 12th International Conference on Ubiquitous Robots and Ambient Intelligence (URAI), Goyang, Republic of Korea, 28–30 October 2015; IEEE: Piscataway, NJ, USA, 2015; pp. 460–461. [[CrossRef](#)]
53. Navarro, M.; Najar, M. TOA and DOA estimation for positioning and tracking in IR-UWB. In Proceedings of the 2007 IEEE International Conference on Ultra-Wideband, Sydney, Australia, 27–30 August 2007; IEEE: Piscataway, NJ, USA, 2007; pp. 574–579. [[CrossRef](#)]
54. Liu, F.; Li, X.; Wang, J.; Zhang, J. An Adaptive UWB/MEMS-IMU Complementary Kalman Filter for Indoor Location in NLOS Environment. *Remote. Sens.* **2019**, *11*, 2628. [[CrossRef](#)]
55. Agrawal, M.; Konolige, K. Real-time localization in outdoor environments using stereo vision and inexpensive gps. In Proceedings of the 18th International Conference on Pattern Recognition (ICPR'06), Hong Kong, China, 20–24 August 2006; IEEE: Piscataway, NJ, USA, 2006; Volume 3, pp. 1063–1068. [[CrossRef](#)]
56. Pramreiter, M.; Nenning, T.; Malzl, L.; Konnerth, J. A plea for the efficient use of wood in construction. *Nat. Rev. Mater.* **2023**, *8*, 217–218. [[CrossRef](#)]
57. Chuttur, M.; Gillela, S.; Yadav, S.M.; Wibowo, E.S.; Sihag, K.; Rangppa, S.M.; Bhuyar, P.; Siengchin, S.; Antov, P.; Kristak, L.; et al. A comprehensive review of the synthesis strategies, properties, and applications of transparent wood as a renewable and sustainable resource. *Sci. Total. Environ.* **2023**, *864*, 161067. [[CrossRef](#)] [[PubMed](#)]
58. Zou, A.; Hu, W.; Luo, Y.; Jiang, P. An Improved UWB/IMU Tightly Coupled Positioning Algorithm Study. *Sensors* **2023**, *23*, 5918. [[CrossRef](#)]
59. Sola, J. Quaternion kinematics for the error-state Kalman filter. *arXiv* **2017**, arXiv:1711.02508.
60. Sung, S.; Kim, H.; Jung, J.-I. Accurate Indoor Positioning for UWB-Based Personal Devices Using Deep Learning. *IEEE Access* **2023**, *11*, 20095–20113. [[CrossRef](#)]
61. Zhu, W.; Zhao, R.; Zhang, H.; Lu, J.; Zhang, Z.; Wei, B.; Fan, Y. Improved Indoor Positioning Model Based on UWB/IMU Tight Combination with Double-Loop Cumulative Error Estimation. *Appl. Sci.* **2023**, *13*, 10046. [[CrossRef](#)]

**Disclaimer/Publisher’s Note:** The statements, opinions and data contained in all publications are solely those of the individual author(s) and contributor(s) and not of MDPI and/or the editor(s). MDPI and/or the editor(s) disclaim responsibility for any injury to people or property resulting from any ideas, methods, instructions or products referred to in the content.